Monthly Notices of the ROYAL ASTRONOMICAL SOCIETY

MNRAS **543,** 2349–2373 (2025) https://doi.org/10.1093/mnras/staf1490
Advance Access publication 2025 September 8

Investigating the Upper Scorpius OB association with HERMES – I. The spectroscopic sample and 6D kinematics

Joseph J. Armstrong [1★] Jonathan C. Tan,[1] Nicholas J. Wright [2] R. D. Jeffries [2] Janez Kos [3] E. Fiorellino,[4,5] Sven Buder [6,7,8] and D. Barrios López[9]

[1]*Department of Space, Earth & Environment, Chalmers University of Technology, SE-412 96 Gothenburg, Sweden*
[2]*Astrophysics Group, Keele University, Keele ST5 5BG, UK*
[3]*Faculty of mathematics and physics, University of Ljubljana, Jadranska 19, 1000 Ljubljana, Slovenia*
[4]*Alma Mater Studiorum – Universit. di Bologna, Dipartimento di Fisica e Astronomia "Augusto Righi", Via Gobetti 93/2, I-40129, Bologna, Italy*
[5]*INAF–Osservatorio Astronomico di Trieste, via Tiepolo 11, I-34143 Trieste, Italy*
[6]*Research School of Astronomy and Astrophysics, Australian National University, Canberra, ACT 2611, Australia*
[7]*ARC Centre of Excellence for All Sky Astrophysics in 3 Dimensions (ASTRO 3D), Australia*
[8]*ACCESS-NRI, Australian National University, Canberra, ACT2601, Australia*
[9]*Instituto de Estudios Astrofísicos, Facultad de Ingeniería y Ciencias, Universidad Diego Portales, Av. Ejército Libertador 441, Santiago, Chile*

Accepted 2025 July 15. Received 2025 July 11; in original form 2025 May 16

ABSTRACT

OB associations are large, unbound groups of young stars, which typically exhibit great complexity in spatial, kinematic and age structure, hinting at formation scenarios involving an intricate interplay of molecular cloud turbulent kinematics and stellar feedback over extended periods. The kinematic properties of the numerous low-mass populations within OB associations can provide valuable constraints on their initial configurations, and thus the dominant mechanisms driving star formation and their dispersal into the field. We present results from a large spectroscopic survey of the nearest young association to the Sun, Upper Scorpius, conducted using 2dF/HERMES on the Anglo-Australian Telescope. We use spectroscopic youth criteria such as Li-equivalent widths to identify >1000 pre-main sequence (PMS) members across the region and measure radial velocities, combining these with *Gaia* EDR3 5-parameter astrometry to obtain 6D kinematic information. We separate confirmed PMS association members into distinct kinematic groups and measure expansion and rotation trends in each. We also trace the past motion of these groups using an epicycle approximation and estimate the time since their most compact configuration. These kinematic properties are compared to literature ages and the star formation history of Upper Scorpius is discussed. We find evidence that a scenario in which star formation in the subgroups of Upper Scorpius proceeded independently, either by self-instability or external feedback from Upper Centaurus-Lupus, is more likely than a recently proposed 'cluster chain' scenario in which these subgroups have triggered each other.

Key words: techniques: spectroscopic – Surveys – stars: kinematics and dynamics – stars: pre-main-sequence – open clusters and associations: individual: Upper Scorpius.

1 INTRODUCTION

Most stars form in dense, gravitationally bound clusters or sparse substructured associations (e.g. Lada & Lada 2003; Wright et al. 2023). Apart from the brightest O & B type stars, by which OB associations were first identified (Ambartsumian 1947; Blaauw 1964; de Zeeuw et al. 1999), the sparse distributions of low-mass young stellar objects (YSOs) that accompany them have historically been harder to detect. In addition, they tend to be unbound and thus disperse into the Galactic field over time-scales of a few tens of Myrs (Wright 2020).

Recent investigations, particularly using high-precision astrometry from *Gaia* (Gaia Collaboration 2016, 2021), have been able to identify the sparse and highly substructured distributions of nearby associations (e.g. Wright et al. 2016; Wright & Mamajek 2018; Zari, Brown & de Zeeuw 2019; Cantat-Gaudin et al. 2019a; Armstrong et al. 2022). Associations have also been revealed to contain significant age gradients (Kounkel et al. 2018; Damiani et al. 2019; Kos et al. 2019; Cantat-Gaudin et al. 2019b; Ratzenböck et al. 2023b), which, along with significant kinematic structure (Wright et al. 2016; Wright & Mamajek 2018; Armstrong et al. 2022; Miret-Roig et al. 2022b; Kerr et al. 2025), indicates complex star formation histories involving the impact of feedback processes and turbulence within molecular clouds to produce initially unbound distributions of young stars in large volumes. This is in contrast to the monolithic cluster formation model where stars form in initially compact configurations, but disperse after residual gas expulsion (Tutukov 1978; Hills 1980; Kroupa, Aarseth & Hurley 2001), which

★ E-mail: jarmstrongastro@gmail.com

would imply that OB associations are an intermediate stage of cluster dissolution.

However, it has yet to be determined what are the dominant mechanisms driving star formation in these complexes. It has been suggested that the age gradients found in OB associations point towards multiple epochs of star formation, with the initiation of star formation in one epoch being triggered by the impact of feedback from massive stars formed in the previous epoch (e.g. Elmegreen & Lada 1977; Kerr et al. 2025; Posch et al. 2025). There is also the suggestion that star formation could be initiated by collisions between giant molecular clouds (GMCs; e.g. Scoville, Sanders & Clemens 1986), with a model in which collisions are driven by galactic shearing motions of orbiting GMCs (Tan 2000; Tasker & Tan 2009; Li et al. 2018) being potentially relevant to explaining observed large-scale star formation properties of disc galaxies (Tan 2010; Suwannajak, Tan & Leroy 2014; Fortune-Bashee, Sun & Tan 2024). Simulations of star formation resulting from individual GMC–GMC collisions, with relative cloud velocities of $\sim 10\,\mathrm{km\,s^{-1}}$ can produce spatial structure and disturbed kinematics among the newly formed stars similar to those observed in nearby regions (e.g. Wu et al. 2017, 2020). Stellar feedback driven cloud collisions have also been proposed as the main driver of new star formation in galaxies (Inutsuka et al. 2015). Other possibilities include models of star formation regulated by turbulence in GMCs (e.g. Krumholz & McKee 2005; Hennebelle & Chabrier 2011; Padoan & Nordlund 2011). Combinations of the above models are also possible, e.g. if shear-driven GMC collisions are the main driver of turbulence in GMCs (Tan, Shaske & Van Loo 2013; Wu et al. 2018).

Upper Scorpius is the youngest (≈11 Myr; Pecaut & Mamajek 2016) subgroup within Scorpius–Centaurus, the nearest OB association to the Sun (100–150 pc; de Zeeuw et al. 1999), containing > 100 OB stars spread over ≈200 square deg. Its proximity, youth and low extinction make it a prime target for studies of the low-mass population of OB associations, even to the brown-dwarf regime (Wright & Mamajek 2018; Damiani et al. 2019; Luhman & Esplin 2020). The low extinction for association members indicates that the association has dispersed from its primordial molecular cloud. Recent kinematic studies show that Upper Sco is highly kinematically substructured and almost certainly unbound (Wright & Mamajek 2018; Squicciarini et al. 2021). The full extent of the low-mass population is currently unknown, but thousands of low-mass counterparts to the OB population should exist for a normal initial mass function (IMF; e.g. Kroupa 2001; Chabrier 2003). The velocity dispersion ($\approx 3.2\,\mathrm{km\,s^{-1}}$; Wright & Mamajek 2018) and age (≈11 Myr; Pecaut & Mamajek 2016) of the known PMS and OB stars, and total spatial extent (≈40 pc; Wright & Mamajek 2018) of Upper Sco seem incompatible with the simple expansion of a monolithic cluster after gas expulsion, and in fact Wright & Mamajek (2018) could not find evidence that the association had expanded from a single compact cluster. Instead, a hypothesis is that Upper Sco formed hierarchically at various sites, perhaps in a sequential way, so that there is a widespread population of unbound PMS stars dispersed across the association, while the massive stars may coincide with bound subclusters with unique kinematics (Damiani et al. 2019).

Recently the clustering and kinematics of Upper Scorpius have been investigated using high-precision astrometry from *Gaia* (Gaia Collaboration 2021) with the finding that Upper Scorpius can indeed be divided into multiple subgroups (Squicciarini et al. 2021; Miret-Roig et al. 2022b; Ratzenböck et al. 2023b), which differ in their kinematics and ages, with older subgroups being centrally located within the Upper Scorpius region and younger subgroups located at the outskirts. This has led to the proposed 'cluster chain' formation scenario (Posch et al. 2025) which hypothesises that the formation of the younger subgroups was triggered by feedback from the older subgroups in sequence. This would produce a significant age gradient across the region, as well as the large-scale 'acceleration' observed between these subgroups.

However, these previous kinematic studies have gathered the majority of their radial velocity information from public surveys, such as APOGEE (Ahumada et al. 2020) and GALAH (Buder et al. 2021), which vary in radial velocity precision and in coverage across the region, meaning that the internal 3D kinematics of much of the low-mass population has not yet been fully analysed. Also, in these studies, membership for the bulk of the low-mass population of Upper Sco has so far been determined using astrophotometric or kinematic criteria, which risks biasing sample selection and analysis away from sources and structures with kinematics distinct from the bulk of the region. Ideally, membership determination and target selection for further observations should be kinematically unbiased in order to investigate the full complexity of the region. In particular, spectroscopic observations are necessary to provide both the missing radial velocities and firm youth criteria, such as Li-equivalent widths, enabling us to perform membership determination for young stars in the region independent of the kinematics we wish to analyse.

In this study, we present results from a large-scale spectroscopic survey across the Upper Scorpius region with the goal of identifying young stars and studying their kinematics. Section 2 outlines the data used and the spectroscopic observations performed. Section 3 provides an overview of the region and dissects the young stellar population into distinct kinematic groups, with Section 5 going on to analyse their internal dynamics, focusing on expansion trends, kinematic anisotropies, and kinematic age estimates via dynamical traceback. In particular, we look for evidence that the subgroups in the region are unbound and were likely in more compact configurations in the past, with the goal of assessing whether they could have formed as a sequence of dense clusters, or whether it is more likely that they formed in sparse distributions. In Section 6, we discuss our results in light of recent literature and infer the likely star formation scenario of the Upper Scorpius association.

2 THE DATA

In this section, we describe the target selection for spectroscopic observations with 2dF/AAT, and derivation of spectroscopic parameters, which we combined with astrometric and photometric data from *Gaia* to produce our sample of young stars with complete kinematic information.

2.1 AAT observations

We selected candidate PMS stars in the Upper Sco region for spectroscopic follow-up using a *Gaia* DR3 G_{BP}–G_{RP} versus M_G colour–absolute magnitude diagram (using distance estimates from Bailer-Jones et al. 2021) and selecting sources located above a 20 Myr PMS isochrones (Baraffe et al. 2015, see Fig. 1), with $13 < G < 16.5$ and $\varpi > 2.5$ mas (<400 pc) to filter out background contaminants.

We selected targets in 25 fields (Fig. 2; listed in Table 1), which cover the densest groups of likely young stars in the region, as indicated by our photometric selection (Fig. 1) and by *Gaia* DR3 variability criteria (Marton et al. 2023), and effectively sample the distinct populations present in the region (Luhman & Esplin 2020; Miret-Roig et al. 2022b; Ratzenböck et al. 2023b).

Observations were made on April 16th, May 21st–22nd and June 10th–12th 2023 with the 2-deg field (Lewis et al. 2002; 2dF)

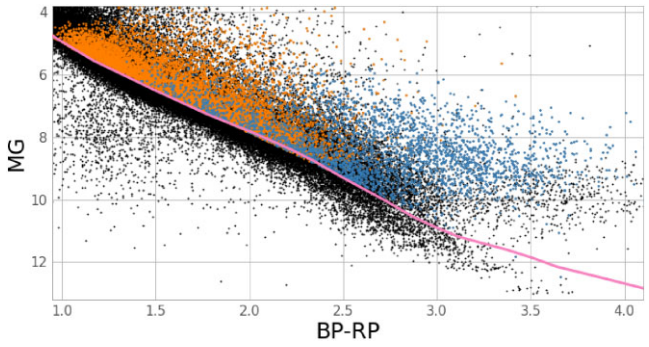

Figure 1. *Gaia* DR3 BP–RP colour versus absolute G magnitude for sources in the Upper Sco region with $13 < Gmag < 16.5$ and $\varpi < 5$ (blue) or $\varpi < 2.5$ (orange). Absolute magnitudes are calculated using distance estimates from Bailer-Jones et al. (2021) and average A_G and E(BP–RP) values from *Gaia* DR2 per 0.25 deg^2 square by 50 pc los-distance volume, similar to the method employed by Zari et al. (2019). Overplotted is the 20 Myr PMS isochrone (pink) from Baraffe et al. (2015).

fibre positioner and the high-efficiency and resolution multielement spectrograph (Sheinis et al. 2015; HERMES), which provides a resolution of $R \sim 28\,000$ in four optical bands, at the Anglo-Australian Telescope (AAT) as part of programme 2023A/30. The red band of HERMES covers the wavelength range 6478–6737 Å within which both the H α 6562.8 Å and Li 6707.8 Å lines are found. For each field we selected > 300 targets based on colour–absolute magnitude diagram (CaMD) position, which totaled 8061 targets for all fields with overlap, 7039 of which were unique sources. Multiple 1800s exposure were taken for each field, the total time for which, along with numbers of targets and numbers of spectroscopically confirmed PMS stars (Section 2.1.3), are given in Table 1. Calibration frames, including dark frames and multifibre flat fields were taken for each field and 25–40 fibres were used to measure the sky spectrum for each field.

2.1.1 *Data reduction and analysis*

The spectroscopic data were calibrated and reduced using the 2dF Data Reduction (2DFDR) software tool (AAO Software Team 2015). Measurement of spectroscopic parameters (equivalent widths of the Li 6707.8 Å line; EW(Li)s) from reduced spectra was done using the same approach as described in Armstrong et al. (2022), following the procedures of Jeffries et al. (2021). We produced synthetic spectra using the MOOG spectral synthesis code (Sneden et al. 2012), with Kurucz (1992) solar-metallicity model atmospheres, for log$g$ = 4.5 and down to $T_{\rm eff}$ = 3500 K in 100 k steps, with rotational broadening and instrument resolution accounted for in the extraction profile.

2.1.2 *Radial velocities*

Radial velocities are the last component of complete 6D position–velocity information missing from *Gaia* for most sources. With high-resolution spectra from HERMES, we can measure radial velocities up to a typical precision of 0.1 km s^{-1} (Zwitter et al. 2018), which is sufficient to investigate the internal kinematics of young clusters and star-forming regions.

The spectra we obtained in these observations have been included in the GALAH survey data release 4 (Buder et al. 2024). Among the many parameters derived are RVs, which we incorporate into our data sample for kinematic analysis. However, not all candidate YSO members of Upper Sco we observed necessarily have RVs in GALAH DR4, due to the various quality controls imposed in the compilation of the catalogue. Therefore, we also derive RVs and uncertainties from our own reduced spectra using the same approach as described in Armstrong et al. (2022).

Reduced target spectra were cross-correlated with their best-fitting synthetic spectra and RVs were determined from the position of the peak in the cross-correlation function (CCF) by fitting a Gaussian function. Targets for which a Gaussian function cannot be satisfactorily fitted to the CCF are not given valid RVs and are rejected from our sample.

RV uncertainties were also determined using the same approach as described in Armstrong et al. (2022), by measuring the change in RV between n separate exposures of the same target ($E_{RV} = \Delta RV/\sqrt{n}$), normalized per field using the scaling function (equation 1; Armstrong et al. 2022).

We also cross-match our sources with the *Survey of surveys* catalogue (Tsantaki et al. 2022), which contains calibrated RVs for over 11 000 000 *Gaia* sources, compiled from multiple spectroscopic surveys. We find RVs for 874 of our targets; 605 with RVs from APOGEE (Majewski et al. 2017), 38 with RVs from the Gaia-ESO survey (Gilmore et al. 2012) and 295 with RVs from Gaia, with overlap.

We find 4006 of our targets with RVs < |200| km s^{-1} and SNR > 10 from both the GALAH DR4 catalogue and our analysis, with a median offset of 0.084 km s^{-1}. We also find 386 targets with RVs < |200| km s^{-1} from both GALAH DR4 (SNR > 10) and the *Survey of surveys* catalogue (Tsantaki et al. 2022), with a median offset of 0.459 km s^{-1}. We calibrate the compiled RVs by applying these offsets to RVs from the relevant source catalogues. For the targets with multiple RVs, we take the weighted mean RVs, weighted by the square of the inverse measurement uncertainties in each case, with the aforementioned RV offsets applied.

In total, we have RVs available for 6727 of our 7039 unique targets, the distribution of which is plotted in Fig. 3.

2.1.3 *Identifying YSOs*

The presence of Li is an effective indicator of youth in low-mass young stars (Soderblom 2010). We measured the equivalent width of the Li 6707.8 Å line (EW(Li)) following the same approach as described in Armstrong et al. (2022), by subtracting the synthetic spectrum from the target spectrum and then integrating under the relevant profile. EW(Li) uncertainties are taken as the RMS value of the EWs measured using the same procedure with the Gaussian profile of the CCF centred at five wavelengths either side of the Li 6707.8 Å line (Jackson, Deliyannis & Jeffries 2018).

We obtained values of EW(Li) and EW(Li) uncertainties for 6937 (98.6 per cent) of our 7039 unique targets, the distribution of which is illustrated in Fig. 4, and we identify 999 YSOs that pass the youth criteria of EW(Li)–EW(Li)_error > 100 mÅ.

Due to veiling, EW(Li)s can be underestimated for YSOs with high mass accretion rates ($\dot{M}_{acc} > 10^{-9}$ M$_\odot$ yr^{-1}, Palla et al. 2005; Frasca et al. 2017), so we also measure spectroscopic signatures of accretion to identify such YSOs, in particular, excess emission of the H α line at 6562.8 Å.

As in Armstrong et al. (2022), we use both the equivalent-width of H α and the spectral index α_w of the wing components of the H α emission profile, as described by Damiani et al. (2014), to select likely Classical T Tauris (CTTs). We adopt thresholds of EW(H α) –

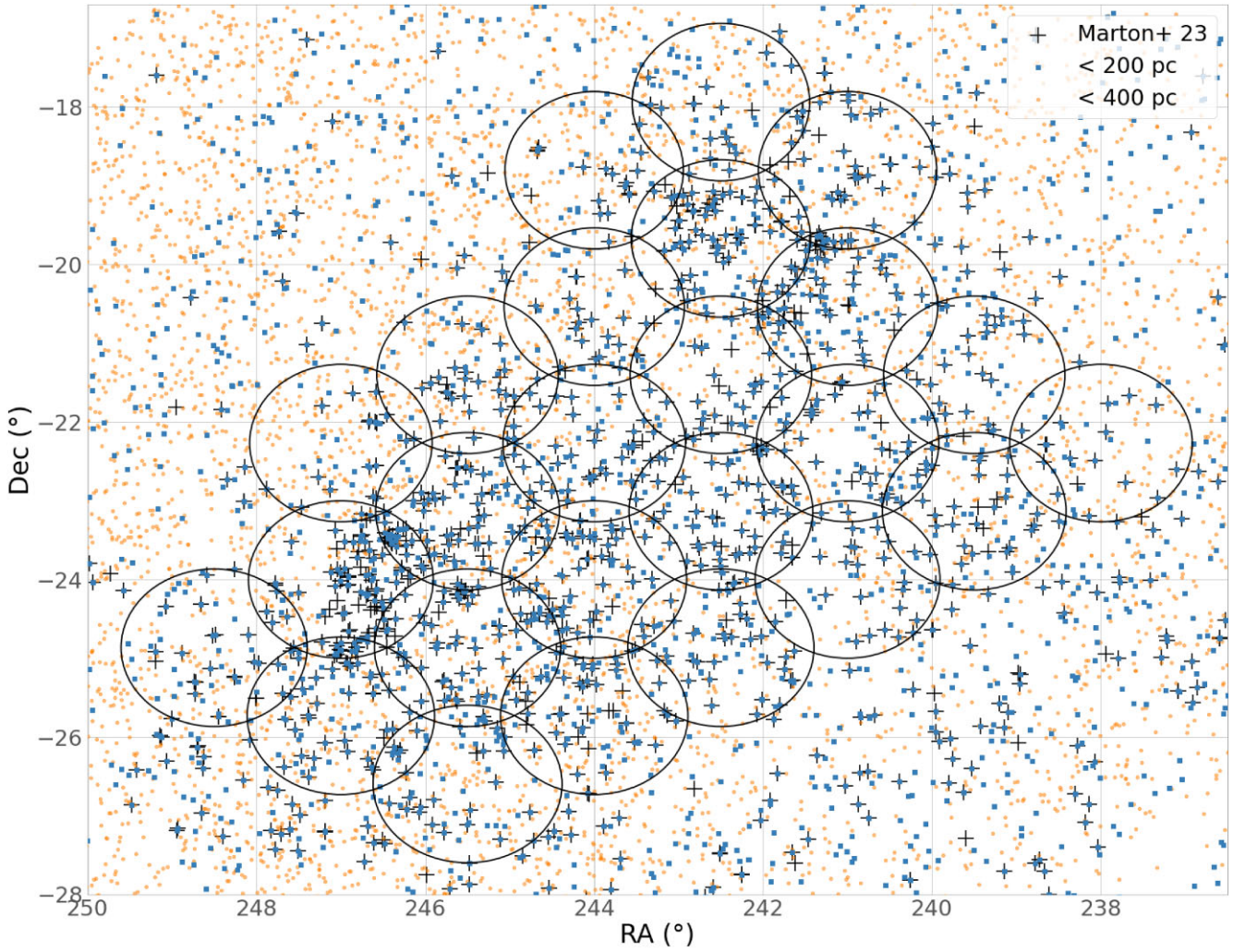

Figure 2. Sky positions of photometrically selected targets colour-coded by their priority (Fig. 1). Sources identified as YSOs by variability in *Gaia* DR3 (Marton et al. 2023) are indicated with plus symbols. The 2°-diameter circles indicate the individual fields of observation of the AAT within which targets were selected. The fields were distributed to effectively cover the region of Upper Scorpius with the greatest density of likely YSOs.

EW(Hα)_error $>$ 10 Å and $\alpha_w > 1.1$ (for sources with $SNR > 5$). We identify 230 YSOs (likely CTTs) in our sample via these Hα criteria, 62 of which did not meet the EW(Li) criteria of EW(Li)–EW(Li)_error $>$ 100 mÅ.

We also cross-match spectroscopic targets with YSOs from the *Gaia* DR3 variability catalogue (Marton et al. 2023). One of the main reasons why YSOs are expected to exhibit optical variability is as a result of fluctuating accretion activity while there remains a circumstellar disc. We identify 986 likely YSOs via this variability criteria, 176 of which we identify as CTTs by our Hα criteria and 831 which are also confirmed as YSOs via EW(Li).

Thus, in total, we identify 1204 YSOs.

2.2 *Gaia* astrometry

Spectroscopic targets are matched to the *Gaia* DR3 catalogue (Gaia Collaboration 2021) to obtain positions, proper motions and parallaxes. Combined with our RVs, this gives us full 6D kinematic information for all of our 1204 confirmed YSOs. We filter targets with poor *Gaia* astrometric quality following the recommended criteria of Fabricius et al. (2021); RUWE $>$ 1.4, *ipd_frac_multi_peak* $>$ 3 and *ipd_gof_harmonic_amplitude* $>$ 0.1, in order to remove non-single stars. The velocity contribution of binary orbits, in particular, could bias our kinematic analysis. We also remove targets with RV$>$ |200| km s^{-1} or with RV uncertainty $>$ 1 km s^{-1}, in order to further filter sources with unreliable RVs and possible binaries. Out of our 1204 confirmed YSOs, 79 fail the *ipd_gof_harmonic_amplitude* criterion, 92 fail the *ipd_frac_multi_peak* criterion, 251 fail the RUWE criterion and 482 fail the RV criteria, with overlap. After applying these astrometric quality filters we are left with 544 confirmed YSOs with quality 6D kinematic information.

2.3 Deriving 3D positions and velocities

We obtain Cartesian positions XYZ and velocities UVW in the Galactic system following the same approach as Armstrong et al. (2022), using the coordinate transformation matrices from Johnson & Soderblom (1987). This is done via Bayesian inference where we perform 1000 iterations with 100 walkers in an unconstrained parameter space. We sample the posterior distribution using the MCMC sampler *emcee* (Foreman-Mackey et al. 2013), reporting the

Table 1. Details of the fields targeted and observed, listing the central coordinates, total exposure time(s), number of science targets and number of confirmed PMS stars per field. As there are some targets included in overlapping fields, the total number of unique targets are given in bold.

Field number	RA (°)	Dec. (°)	Exposure time (s)	Targets	Confirmed YSOs
1	244.0	−24.0	5400	321	88
2	244.0	−22.268	5400	328	59
3	245.5	−23.134	6210	325	107
4	245.5	−24.866	9000	321	108
5	244.0	−25.732	9000	314	57
6	242.5	−24.866	5400	321	67
7	242.5	−23.134	5400	314	71
8	244.0	−20.536	7200	321	33
9	245.5	−21.402	5400	314	38
10	247.0	−22.268	5400	321	25
11	247.0	−24.0	5400	313	133
12	247.0	−25.732	3600	326	96
13	245.5	−26.598	9000	324	47
14	241.0	−24.0	5400	328	41
15	241.0	−22.268	5400	324	65
16	242.5	−21.402	5400	324	62
17	244.0	−18.804	5400	324	31
18	248.5	−24.866	5400	328	47
19	239.5	−23.134	5400	328	56
20	239.5	−21.402	5400	324	30
21	241.0	−20.536	11 520	327	67
22	242.5	−19.670	5400	324	86
23	241.0	−18.804	5400	324	60
24	242.5	−17.938	10 800	328	24
25	238.0	−22.268	5400	324	24
Total				8061 (**7039**)	1522 (**1204**)

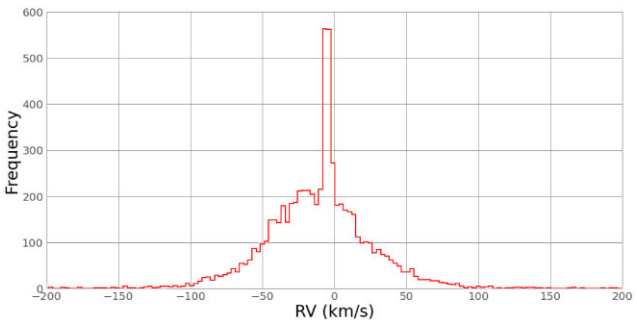

Figure 3. Histogram of calibrated radial velocities (RVs) for 6727 sources in our sample of HERMES targets.

median, 16th and 84th percentiles as the best fit and 1σ uncertainties respectively, after discarding the first 500 iterations as a burn in.

When deriving 3D positions we use *Gaia* parallaxes rather than distance estimates from Bailer-Jones et al. (2021). As described in Fiorellino et al. (2024), the priors involved in the probabilistic estimation of distances by Bailer-Jones et al. (2021) are not optimized for YSOs, nor for sources in clustered regions. We apply the parallax zero point correction to our sources, as prescribed in Lindegren et al. (2021), as a function of ecliptic latitude, magnitude and colour. We also apply the magnitude dependent correction to parallax uncertainties prescribed by El-Badry, Rix & Heintz (2021).

2.4 Summary of the data

After reducing the spectra of our AAT sources, we have 6646 unique sources with spectroscopic RV and EW(Li) values spread across 25 fields over the Upper Sco region, with 5-parameter astrometry from *Gaia* EDR3, with which we calculate Cartesian XYZ positions and UVW velocities. 1204 of these sources are identified as YSOs with significant EW(Li)s, EW(Hα)s or *Gaia* variability flag. The median uncertainties on parallax, distance, proper motion and RV for the confirmed PMS stars are 0.05 mas, 0.9 pc, 0.05 mas yr^{-1} and 0.56 km s^{-1} respectively, with a median SNR = 16.1 of their HERMES spectra. 544 of these confirmed PMS stars pass our filters for astrometric quality.

3 OVERVIEW OF THE SAMPLE

Fig. 5 shows the spatial distribution of the 1204 confirmed YSOs with their proper motion vectors colour-coded according to their relative proper motion (relative to the median of the sample). It is immediately apparent that there are multiple subgroups among the YSOs with distinct bulk proper motions, as well as a number of high proper motion YSOs seemingly unassociated with any of the major groups. The distribution of YSOs in proper motion space and line-of-sight (LOS) distance versus RV space is plotted in Fig. 6. There is also apparent spatial and velocity structure along the LOS, with the bulk of the YSO population located at $\sim$ 140 pc, but also a smaller concentration at $\sim$ 155 pc, as well as a sparse distribution up to $\sim$ 40 pc in the foreground.

We compare our sample of confirmed YSOs to previously compiled catalogues of candidate YSOs in Upper Sco to assess their relative completeness and to highlight the advantages of different methods of YSO identification.

3.1 Cross-match with Miret-Roig et al. (2022b)

Miret-Roig et al. (2022b) used a Gaussian mixture model to separate the Upper Sco and Ophiuchus YSO candidate list of Miret-Roig

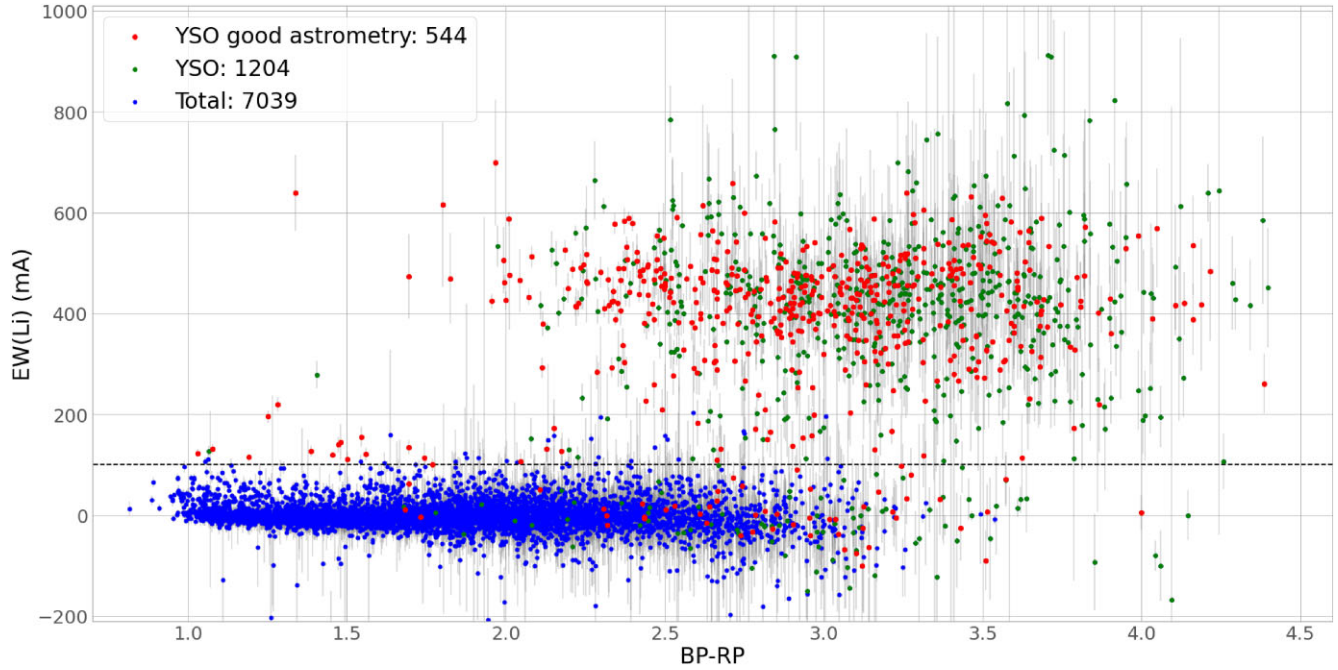

Figure 4. Equivalent width of the lithium 6708 Å line plotted against the *Gaia* DR3 BP–RP colour. Sources that pass one or more of our YSO criteria are plotted in green, sources that pass one or more of our YSO criteria, and also pass our astrometric quality criteria are plotted in red, sources that meet no YSO criteria are plotted in blue (likely non-YSOs). The EW(Li) threshold value for selecting YSOs (100 mÅ) is indicated with a dashed line.

et al. (2022a) into kinematically distinct subgroups. Out of our full target sample we find 1065 matches with the members of Upper Sco identified by Miret-Roig et al. (2022b) using the HDBSCAN algorithm. 228 belong to α Sco, 98 belong to β Sco, 199 belong to δ Sco, 119 belong to π Sco, 85 belong to ν Sco, 197 belong to ρ Oph, 139 belong to σ Sco. Also, 946 of these are identified as YSOs in the *Gaia* variability catalogue (Marton et al. 2023), and 946 have RVs in our sample.

Considering our 1204 confirmed YSOs, we find 1030 matches with the members of Upper Sco identified by Miret-Roig et al. (2022b). 224 belong to α Sco, 98 belong to β Sco, 198 belong to δ Sco, 94 belong to π Sco, 84 belong to ν Sco, 197 belong to ρ Oph, 135 belong to σ Sco. The remaining 174 YSOs were not identified as members of any subgroup by Miret-Roig et al. (2022b), and we discuss their membership in Section 4. There are also 5 subgroup members of Miret-Roig et al. (2022b) for which we have spectra of SNR$>$ 20, but do not meet any of our YSO criteria. The number of false-negatives in particular highlights the importance of spectroscopic youth indicators for identifying YSOs with kinematics distinct from the major subgroups.

Out of our 544 confirmed YSOs with quality 6D kinematic information, we find 493 matches with the members of Upper Sco identified by Miret-Roig et al. (2022b). 111 belong to α Sco, 53 belong to β Sco, 110 belong to δ Sco, 35 belong to π Sco, 43 belong to ν Sco, 93 belong to ρ Oph, 48 belong to σ Sco. The remaining 51 YSOs were not allocated to any subgroup by Miret-Roig et al. (2022b), and we discuss their membership in Section 4.

Fig. 9 shows the spatial distribution of the 1204 confirmed PMS stars indicated with plus symbols, as well as the positions of 1580 Upper Sco subgroup members of Miret-Roig et al. (2022b) within the same magnitude range as our observed sample ($13 < G < 16.5$), colour-coded according to their subgroup membership. The AAT FOVs are indicated by the overlaid circles.

It is important to note that the FOVs coverage of each subgroup varies. β, ν Sco, and ρ Oph are almost completely covered, while δ, π and σ Sco have many members that lie outside the observed region, towards Lupus and Upper Centaurus-Lupus (UCL). Therefore, the central positions of these subgroups in our sample will differ from those given by Miret-Roig et al. (2022b), but our sample should still be sufficient to measure kinematic properties.

3.2 Cross-match with Ratzenböck et al. (2023b)

Ratzenböck et al. (2023b) selected a large sample of candidate YSOs across Sco-Cen, including Upper Sco, from the Gaia DR3 catalogue using photometric cuts and astrometric quality criteria. They then identify kinematically distinct subgroups using the SIGMA clustering algorithm (Ratzenböck et al. 2023a).

Out of our full target sample we find 1121 matches with the members of Sco-Cen (including Upper Sco) identified by Ratzenböck et al. (2023b) using the SIGMA algorithm. 217 belong to ρ Oph, 79 belong to ν Sco, 276 belong to δ Sco, 121 belong to β Sco, 165 belong to σ Sco, 157 belong to Antares, 54 belong to ρ Sco, 52 belong to US-foreground. Also, 960 of these are identified as YSOs in the *Gaia* variability catalogue (Marton et al. 2023), and 994 have RVs in our sample.

Out of our 1204 confirmed YSOs we find 1085 matches with the members of Sco-Cen identified by Ratzenböck et al. (2023b). 216 belong to ρ Oph, 78 belong to ν Sco, 272 belong to δ Sco, 121 belong to β Sco, 161 belong to σ Sco, 154 belong to Antares, 52 belong to ρ Sco, 31 belong to US-foreground. The remaining 119 YSOs were not identified as members of any subgroup by Ratzenböck et al. (2023b), likely because their kinematics are too distinct from the subgroups for the SIGMA algorithm to allocate them. There are also 7 subgroup members of Ratzenböck et al. (2023b) for which we have spectra of SNR $>$ 20 , but do not meet any of our YSO criteria. 29 more of

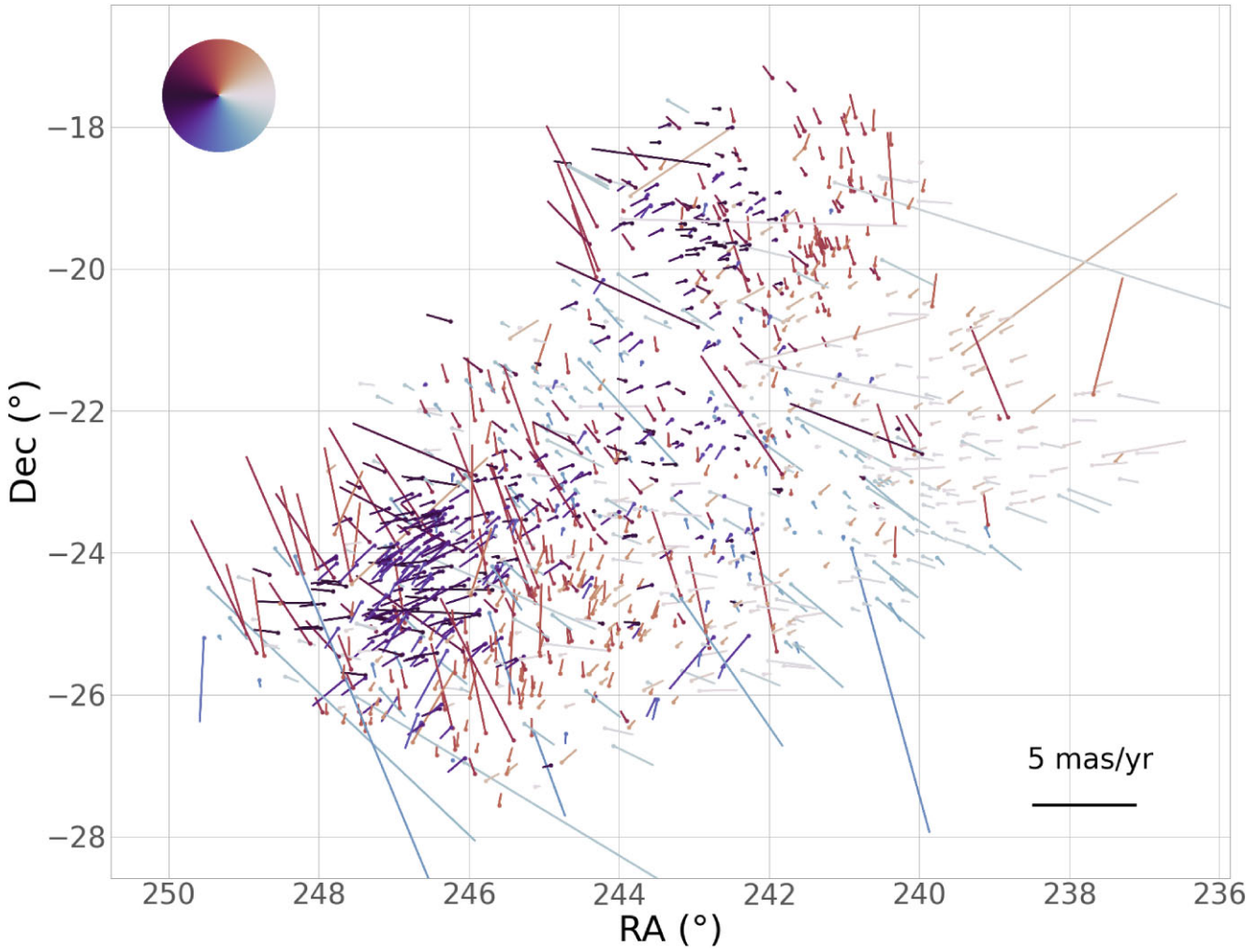

Figure 5. Sky positions of confirmed YSOs observed with the AAT. Vectors indicate the proper motion of each source relative to the median of all Upper Sco YSOs in the sample, colour-coded based on the position angle of the proper motion (see the colour wheel in the top left as a key). The magnitude scale (mas yr^{-1}) of proper motion vectors is indicated by the scale bar in the bottom right.

our targets with matches to the list of Ratzenböck et al. (2023b) we do not confirm as YSOs, but these have spectra of SNR<5 and so their EW(Li) measurements are relatively uncertain. Again, the number of false-negatives highlights the importance of spectroscopic youth indicators for identifying YSOs independently of their kinematics.

Out of our 544 confirmed YSOs with quality 6D kinematic information, we find 495 matches with the members of Sco-Cen identified by Ratzenböck et al. (2023b). 92 belong to ρ Oph, 36 belong to ν Sco, 138 belong to δ Sco, 55 belong to β Sco, 71 belong to σ Sco, 70 belong to Antares, 24 belong to ρ Sco, 9 belong to US-foreground. The remaining 49 YSOs were not identified as members of any subgroup by Ratzenböck et al. (2023b).

3.3 Cross-match with Luhman (2022)

Luhman (2022) selected likely members of Sco-Cen using Gaia DR3 photometric and astrometric criteria. Out of our total observed sample we find 1009 matches with the members of Sco-Cen identified by Luhman (2022), 1007 of which match with our 1204 confirmed YSOs, and 2, for which we have spectra of SNR>20, do not meet any of our YSO criteria.

4 CLUSTERING

Considering the limitations involved in target selection, and positional bias introduced by the fibre configuration for observations, we do not perform our own clustering analysis of Upper Sco with our spectroscopic sample. Rather, we adopt the subgroups identified by Miret-Roig et al. (2022b).

For the YSOs that we have identified which were not included in the subgroup membership list of Miret-Roig et al. (2022b), we allocate to the group to which its 6D kinematics are most similar. We determine which group a YSO is most similar to using the distance in 6D between the YSO and the group central Cartesian positions (X,Y,Z) and velocities (U,V,W) weighted by the inverse of the group's standard deviation in these coordinates (Fig. 7). The total number of YSO members in each subgroup and the number of new YSOs, either with or without quality 6D kinematic information, are given in Table 2.

We then recalculate the new median and dispersion of each Cartesian coordinate per subgroup using the total number of YSOs

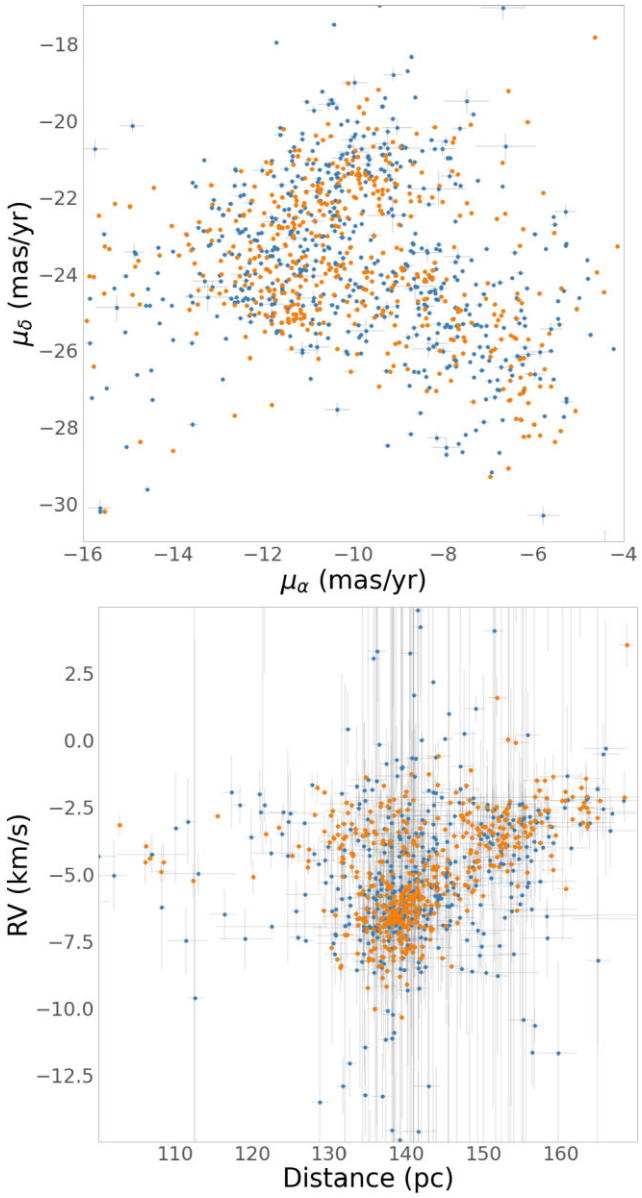

Figure 6. *Top:* Proper motion space and *Bottom:* Bailer-Jones et al. (2021) distance versus RV of confirmed YSOs with quality 6D kinematic information (red) and without (blue).

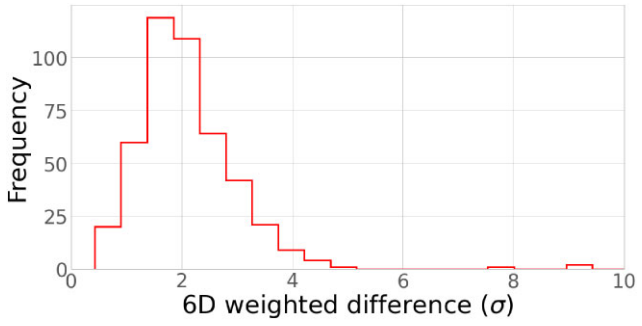

Figure 7. Histogram of 6D weighted distance between YSOs not belonging to a Miret-Roig et al. (2022b) subgroup and their nearest subgroup.

with quality 6D kinematic information and present these with their associated uncertainties in Table 2. In subsequent figures, members of these subgroups are plotted in green for α Sco, blue for β Sco, orange for δ Sco, purple for ν Sco, yellow for π Sco, pink for ρ Oph & red for σ Sco.

For YSOs with significantly distinct kinematics from any group, i.e. 6D weighted difference $> 3\sigma$ (Fig. 7), we keep separately in a group of kinematic outliers, which we investigate later to determine if any might be dynamically ejected YSOs either from Upper Sco or from another nearby young cluster. We find 84 YSOs that we categorize as kinematic outliers. In subsequent figures these are plotted in black.

We re-plot the proper motion distribution and LOS distance versus RV distribution of YSOs in Fig. 8 colour-coded according to the kinematic subgroup they have been allocated to. Most subgroups appear sparse and have significant overlap in proper motion space, but clearer separation is seen in LOS distance versus RV between α Sco (green) and π Sco (yellow) which extend further into the foreground and have greater RVs than δ Sco (orange), ν Sco (purple) and σ Sco (red).

In Fig. 10, we show the Cartesian spatial (XYZ, *top panel*) and velocity (UVW, *lower panel*) structure of the 544 confirmed PMS stars with quality 6D information, colour-coded according to which subgroup they are assigned to.

Notably, all subgroups apart from δ Sco have their largest spatial spread (σ_{XYZ}) in the Cartesian X-direction (Fig. 10). For both α Sco and π Sco, σ_X is more than twice as large as the next greatest, σ_Y, and is different from the spread in σ_Z at the $> 60\sigma$ significance level. We measure the significance of anisotropy by dividing the difference between the largest spatial spread and the smallest to their combined uncertainties for each subgroup. For β Sco, spatial spreads are anisotropic at the 6σ level, for δ Sco, at the 12σ level, for ν Sco, at the 16σ level, for ρ Oph, at the 17σ level and for σ Sco, at the $> 30\sigma$ level.

The Heliocentric Cartesian X coordinate is directed towards the Galactic centre, so for Upper Sco this is the coordinate which contains the greatest component of observed parallax. Thus, parallax uncertainty, and uncertainty in line-of-sight distance, would likely inflate the spread of positions in this direction. However, as Upper Sco is relatively nearby (100–150 pc), the median uncertainty in LOS distance of our confirmed YSOs is relatively small, only 0.9 pc, and thus cannot account for this spatial anisotropy. Rather, limitations in the coverage of observations, particularly the total sky area of observed fields, likely have a greater impact. In Fig. 9, we plot the sky positions of all members of Upper Sco subgroups of Miret-Roig et al. (2022b) along with circles indicating the fields of observation. There are many members of α Sco, π Sco, and σ Sco in particular that were not covered in our observations, which has the effect of reducing the spatial spread in Y and Z relative to X.

Similarly, all subgroups apart from ν Sco have their largest velocity dispersion ($\sigma_{\rm UVW}$) in the Cartesian X-direction (U). This could be due to the effect of unresolved binary orbits contributing to the observed RVs. We analyse this in greater detail in Section 5.1.

The β Sco (blue) and ν Sco (purple) subgroups appear to be the most spatially distinct, having little to no overlap with other subgroups in YZ space, though ν Sco overlaps with δ Sco (orange) in XZ space. However, there is much greater overlap between these subgroups and others in velocity space. There is also an apparent gap between the two subgroups, particularly noticeable in XZ space, with an approximate separation of $\sim$12 pc. Around these subgroups are distributed a number of YSOs with kinematics not closely matching any group, which may be candidate ejected stars with high velocities

Table 2. Properties of the Upper Scorpius subgroups based on our sample of confirmed YSOs with 6D kinematic data.

Group	α	β	δ	ν	π	ρ	σ
YSOs (new)	280 (133)	144 (70)	263 (112)	105 (48)	117 (64)	271 (126)	174 (104)
6D YSOs (new)	201 (91)	88 (35)	184 (74)	76 (33)	63 (29)	162 (69)	111 (63)
median X (pc)	$136.15^{+0.43}_{-0.43}$	$140.27^{+0.21}_{-0.22}$	$130.42^{+0.14}_{-0.14}$	$128.44^{+0.13}_{-0.13}$	$125.21^{+0.39}_{-0.37}$	$132.92^{+0.16}_{-0.16}$	$140.95^{+0.39}_{-0.40}$
σ_X (pc)	$10.94^{+0.10}_{-0.09}$	$2.91^{+0.10}_{-0.10}$	$3.27^{+0.07}_{-0.07}$	$2.11^{+0.05}_{-0.05}$	$11.96^{+0.08}_{-0.08}$	$2.85^{+0.09}_{-0.09}$	$7.53^{+0.10}_{-0.10}$
median Y (pc)	$-19.16^{+0.09}_{-0.08}$	$-16.59^{+0.04}_{-0.03}$	$-21.00^{+0.06}_{-0.07}$	$-12.61^{+0.02}_{-0.02}$	$-17.33^{+0.07}_{-0.07}$	$-15.33^{+0.03}_{-0.04}$	$-21.93^{+0.09}_{-0.10}$
σ_Y (pc)	$4.42^{+0.01}_{-0.01}$	$2.22^{+0.01}_{-0.01}$	$3.10^{+0.01}_{-0.01}$	$1.74^{+0.01}_{-0.00}$	$4.96^{+0.01}_{-0.01}$	$1.30^{+0.01}_{-0.01}$	$3.98^{+0.02}_{-0.02}$
median Z (pc)	$46.09^{+0.10}_{-0.09}$	$61.78^{+0.10}_{-0.10}$	$53.72^{+0.11}_{-0.11}$	$54.63^{+0.06}_{-0.06}$	$44.63^{+0.12}_{-0.12}$	$41.81^{+0.09}_{-0.09}$	$51.79^{+0.12}_{-0.12}$
σ_Z (pc)	$4.33^{+0.03}_{-0.03}$	$2.49^{+0.04}_{-0.04}$	$3.48^{+0.03}_{-0.03}$	$1.23^{+0.02}_{-0.02}$	$4.17^{+0.03}_{-0.03}$	$2.39^{+0.03}_{-0.03}$	$4.62^{+0.03}_{-0.03}$
median U (km s^{-1})	$-3.62^{+0.07}_{-0.07}$	$-2.91^{+0.13}_{-0.12}$	$-6.14^{+0.03}_{-0.03}$	$-5.06^{+0.08}_{-0.08}$	$-4.46^{+0.12}_{-0.12}$	$-5.97^{+0.07}_{-0.07}$	$-4.76^{+0.08}_{-0.07}$
σ_U (km s^{-1})	$2.24^{+0.04}_{-0.04}$	$1.11^{+0.08}_{-0.08}$	$0.94^{+0.01}_{-0.01}$	$0.90^{+0.04}_{-0.04}$	$0.98^{+0.07}_{-0.07}$	$1.36^{+0.04}_{-0.04}$	$1.42^{+0.03}_{-0.03}$
median V (km s^{-1})	$-16.67^{+0.03}_{-0.03}$	$-16.19^{+0.03}_{-0.03}$	$-16.24^{+0.02}_{-0.02}$	$-15.40^{+0.02}_{-0.02}$	$-18.13^{+0.04}_{-0.04}$	$-15.29^{+0.03}_{-0.03}$	$-16.80^{+0.05}_{-0.05}$
σ_V (km s^{-1})	$0.64^{+0.01}_{-0.01}$	$0.48^{+0.02}_{-0.02}$	$0.51^{+0.01}_{-0.01}$	$0.39^{+0.01}_{-0.01}$	$0.44^{+0.02}_{-0.02}$	$0.89^{+0.01}_{-0.01}$	$1.09^{+0.01}_{-0.01}$
median W (km s^{-1})	$-5.90^{+0.03}_{-0.03}$	$-6.77^{+0.06}_{-0.06}$	$-7.62^{+0.02}_{-0.02}$	$-8.49^{+0.04}_{-0.04}$	$-4.02^{+0.05}_{-0.05}$	$-9.56^{+0.04}_{-0.04}$	$-7.10^{+0.05}_{-0.05}$
σ_W (km s^{-1})	$0.93^{+0.01}_{-0.01}$	$0.66^{+0.04}_{-0.04}$	$0.70^{+0.01}_{-0.01}$	$0.91^{+0.02}_{-0.02}$	$0.63^{+0.03}_{-0.03}$	$1.12^{+0.01}_{-0.01}$	$1.09^{+0.01}_{-0.01}$
$\bar{v}_{out}$ (km s^{-1})	$0.11^{+0.04}_{-0.04}$	$0.13^{+0.06}_{-0.06}$	$0.46^{+0.05}_{-0.05}$	$0.16^{+0.09}_{-0.09}$	$0.10^{+0.04}_{-0.04}$	$0.24^{+0.07}_{-0.07}$	$0.45^{+0.10}_{-0.10}$
$v_{out} > 0$ (%)	59	69	83	59	64	72	73
μ_{pmRA} (mas yr^{-1})	$-23.31^{+0.14}_{-0.14}$	$-21.77^{+0.06}_{-0.06}$	$-24.01^{+0.08}_{-0.09}$	$-24.12^{+0.11}_{-0.11}$	$-25.47^{+0.43}_{-0.41}$	$-25.61^{+0.17}_{-0.16}$	$-23.23^{+0.16}_{-0.17}$
σ_{pmRA} (km s^{-1})	$0.51^{+0.03}_{-0.03}$	$0.55^{+0.05}_{-0.05}$	$0.89^{+0.06}_{-0.05}$	$0.76^{+0.08}_{-0.07}$	$1.52^{+0.16}_{-0.14}$	$0.80^{+0.05}_{-0.05}$	$1.19^{+0.10}_{-0.08}$
μ_{pmDec} (mas yr^{-1})	$-11.03^{+0.06}_{-0.06}$	$-9.54^{+0.10}_{-0.10}$	$-11.53^{+0.11}_{-0.11}$	$-9.05^{+0.15}_{-0.16}$	$-16.58^{+0.33}_{-0.34}$	$-6.88^{+0.11}_{-0.11}$	$-10.37^{+0.18}_{-0.18}$
σ_{pmDec} (km s^{-1})	$1.22^{+0.08}_{-0.07}$	$0.37^{+0.04}_{-0.03}$	$0.68^{+0.04}_{-0.04}$	$0.56^{+0.06}_{-0.05}$	$1.85^{+0.21}_{-0.17}$	$1.23^{+0.08}_{-0.07}$	$1.07^{+0.09}_{-0.08}$
μ_{RV} (km s^{-1})	$-3.22^{+0.06}_{-0.05}$	$-3.54^{+0.06}_{-0.06}$	$-6.12^{+0.05}_{-0.06}$	$-6.49^{+0.07}_{-0.07}$	$-3.04^{+0.06}_{-0.06}$	$-6.76^{+0.05}_{-0.07}$	$-4.45^{+0.08}_{-0.06}$
σ_{RV} (km s^{-1})	$0.93^{+0.05}_{-0.09}$	$0.73^{+0.05}_{-0.11}$	$0.90^{+0.04}_{-0.09}$	$0.77^{+0.06}_{-0.11}$	$0.98^{+0.06}_{-0.08}$	$1.15^{+0.04}_{-0.08}$	$1.55^{+0.06}_{-0.10}$
σ_{3D} (km s^{-1})	$1.61^{+0.09}_{-0.11}$	$0.99^{+0.08}_{-0.12}$	$1.44^{+0.08}_{-0.11}$	$1.21^{+0.11}_{-0.14}$	$2.59^{+0.26}_{-0.23}$	$1.86^{+0.10}_{-0.12}$	$2.22^{+0.13}_{-0.15}$
Virial mass (M$\odot$)	2150^{+250}_{-290}	310^{+50}_{-70}	1370^{+150}_{-210}	345^{+63}_{-76}	5600^{+1100}_{-1000}	1020^{+110}_{-130}	4050^{+490}_{-550}
Stellar mass (M$\odot$)	480 ± 16	150 ± 9	310 ± 13	110 ± 8	330 ± 12	480 ± 19	560 ± 19
$\tau_{\rm MST}$ (Myr)	$0.4^{+0.5}_{-0.6}$	$-0.4^{+0.4}_{-0.5}$	$-2.3^{+0.4}_{-0.5}$	$0.2^{+0.3}_{-0.3}$	$0.1^{+0.5}_{-0.5}$	$-0.7^{+0.4}_{-0.3}$	$-1.9^{+0.3}_{-0.3}$
$\tau_{\rm DSum}$ (Myr)	$1.8^{+0.2}_{-0.4}$	$-1.0^{+0.4}_{-0.4}$	$-2.3^{+0.3}_{-0.3}$	$0.1^{+0.3}_{-0.3}$	$-4.2^{+0.8}_{-0.8}$	$-0.5^{+0.2}_{-0.2}$	$-2.3^{+0.5}_{-0.4}$
$r_{50,\tau_{\rm MST}}$ (pc)	$10.5^{+0.2}_{-0.1}$	$3.3^{+0.1}_{-0.1}$	$4.2^{+0.1}_{-0.1}$	$2.6^{+0.1}_{-0.1}$	$9.8^{+0.2}_{-0.3}$	$3.0^{+0.1}_{-0.1}$	$8.4^{+0.1}_{-0.1}$
$r_{90,\tau_{\rm MST}}$ (pc)	$20.3^{+0.4}_{-0.2}$	$6.8^{+0.1}_{-0.1}$	$7.3^{+0.1}_{-0.1}$	$4.7^{+0.1}_{-0.1}$	$24.9^{+0.5}_{-0.4}$	$5.7^{+0.2}_{-0.1}$	$12.8^{+0.1}_{-0.1}$
$r_{50,\tau_{\rm DSum}}$ (pc)	$10.4^{+0.1}_{-0.1}$	$3.2^{+0.1}_{-0.1}$	$4.2^{+0.1}_{-0.1}$	$2.6^{+0.1}_{-0.1}$	$8.3^{+0.2}_{-0.1}$	$3.0^{+0.1}_{-0.1}$	$8.4^{+0.1}_{-0.1}$
$r_{90,\tau_{\rm DSum}}$ (pc)	$20.6^{+0.2}_{-0.1}$	$6.8^{+0.1}_{-0.1}$	$7.3^{+0.1}_{-0.1}$	$4.7^{+0.1}_{-0.1}$	$22.1^{+0.5}_{-0.2}$	$5.7^{+0.1}_{-0.1}$	$12.8^{+0.1}_{-0.1}$

relative to the bulk of Upper Sco, or else may be sparse fringes of the β Sco and ν Sco subgroups.

ρ Oph (pink) is the most densely concentrated subgroup spatially, but then appears to be one of the sparser subgroups in velocity space. It has significant spatial overlap with α Sco (green) and some with π Sco (yellow), but these groups are then the most dissimilar to it in velocity space.

σ Sco (red) is perhaps the most sparsely distributed subgroup in both spatial and velocity spaces. Spatially the bulk of σ Sco is located behind δ Sco in the line of sight, but its fringes also overlap with α, β, π, and ν Sco. Only ρ Oph does not have any members of σ Sco overlapping in 3D.

In Fig. 11, we show the Cartesian spatial–velocity coordinate pairs in each panel (X–U: *top*, Y–V: *middle*, Z–W: *bottom*). In X–U and Y–V, there are visible positive correlations between spatial and velocity coordinates across multiple subgroups, which suggests large-scale expansion across Upper Sco. Again, π Sco (yellow) is a notable exception to these trends, with its members located well outside of the multisubgroup linear trends.

Notably, in Z–W space (Fig. 11, *bottom*) ρ Oph (pink) is clearly separated from the majority of other subgroups, overlapping with only a dozen members of σ Sco and α Sco.

5 KINEMATICS

In Fig. 12, we show the Cartesian spatial coordinates of confirmed YSOs with quality 6D kinematic information, colour-coded according to which subgroup they have been allocated to, with vectors indicating their Cartesian velocities (in km s^{-1}) relative to the sample mean.

There is significant variation in the orientation of vectors for members of the sparse subgroups δ Sco (orange) and σ Sco (red), which is a result of their large scatter in velocity space (as can be seen in Fig. 10 *bottom panels*) as well as proximity to the sample mean velocity.

The more spatially concentrated subgroups β Sco (blue), ν Sco (purple), and ρ Oph (pink) tend to have less variation in the orientation of their velocity vectors, as they have less scatter in velocity space. ρ Oph as a whole is clearly moving away from the centre of Upper Sco, while β and ν Sco appear to be moving primarily away from each other rather than from the centre of Upper Sco.

It can also be seen in Fig. 12 that the majority of members of α Sco (green) and π Sco (yellow) have vectors directed towards the centre of Upper Sco, defying the outward trend followed by the other

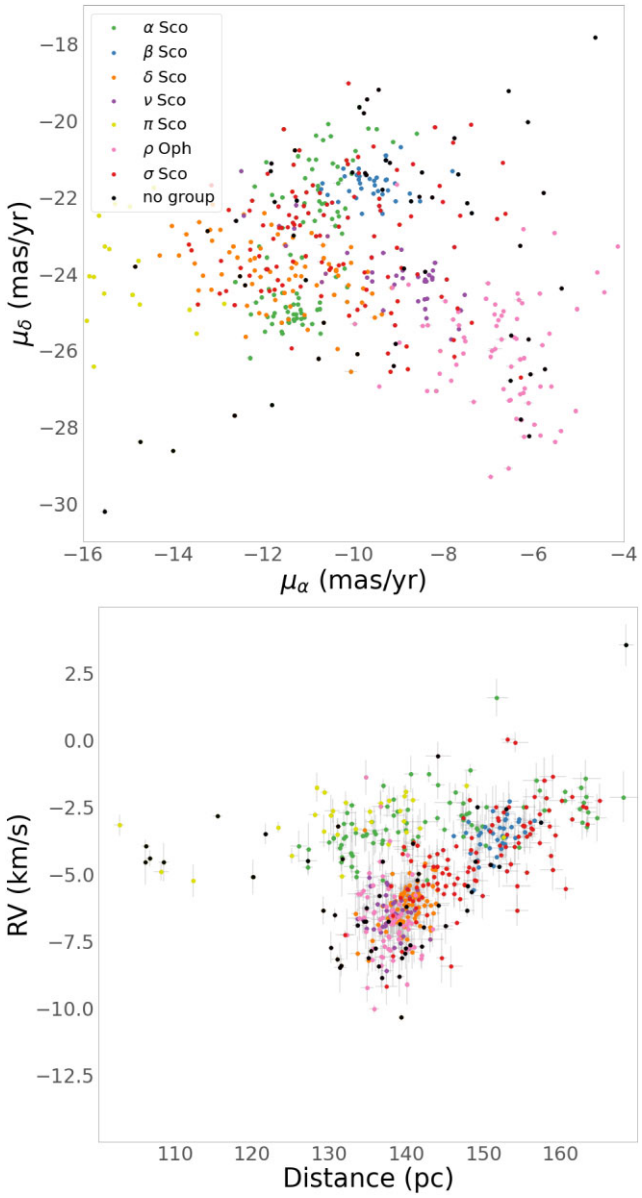

Figure 8. *Top:* Proper motion space and *Bottom:* Bailer-Jones et al. (2021) distance versus RV of confirmed YSOs colour-coded according to the kinematic subgroup they have been allocated to.

subgroups, which is also evidenced by the lack of positive correlation in Cartesian position–velocity space as shown in Fig. 11 (particularly in Z). This indicates that α Sco and π Sco likely have distinct origins from the other Upper Sco subgroups.

In the following analysis, we explore the kinematics of individual subgroups in greater detail.

5.1 Velocity dispersions

Velocity dispersions provide crucial information related to the dynamical state of star clusters and associations. We estimate the velocity dispersions for each group in our sample using a Bayesian approach similar to that described in Armstrong et al. (2022). Where we model the velocity distributions as 3-dimensional Gaussians with the central velocity (μ) and velocity dispersion (σ) in each proper motion and RV as free parameters. We add uncertainties randomly sampled from the observed uncertainty distribution in each dimension for each star.

As in Armstrong et al. (2022), we account for the possible inflation of our RV dispersion due to unresolved binaries by adding velocity offsets to our modelled RVs for 46 per cent of our modelled stars, according to the expected binary fraction (Raghavan et al. 2010). We create a synthetic population of binaries with primary star masses in the range of our observed sample, taken to be 0.65–0.1 $M_\odot$, following a Maschberger (2013) IMF, with secondary star masses randomly sampled with uniform probability from between 0.1–1.0 of their primaries' mass. We sample orbital periods from a lognormal distribution with mean period $log_{10}(5.03)$ and dispersion $log_{10}(2.28)$ d (Raghavan et al. 2010) and we sample eccentricities from a flat distribution between a minimum of $e = 0$ to a maximum scaled with orbital period (Parker et al. 2009). We calculate velocities along the line of sight for each star at random points in their binary orbits at random inclinations in 3D and then weight the velocities of each star per binary by their luminosities.

We do not consider triple systems for the same reasons as given in Armstrong et al. (2022), i.e. their properties are not well constrained and that the RV contribution of third stars is likely to be negligible.

The posterior distribution function is sampled using *emcee* (Section 2.3) and using an unbinned maximum likelihood test. We use uniform priors of -100 to $+100$ km s^{-1} for central velocities and 0 to 100 km s^{-1} for velocity dispersions in each direction. We perform 2000 iterations with 1000 walkers and take the median, 16th and 84th percentile values as the best fit and 1σ uncertainties respectively, after discarding the first 1000 iterations as burn-in.

In Table 2, we list the best fit central velocities μ and velocity dispersions σ for all the seven subgroups of Upper Sco, based on the 544 YSO members with quality filtered 6D kinematic information. Fig. 13 shows the 3D velocity distributions for stars in δ Sco as an example, with the best-fitting velocity dispersion models overplotted in red. We measure the significance of anisotropy by dividing the difference between the largest velocity dispersion and the smallest to their combined uncertainties for each subgroup. The best-fitting velocity dispersions for most subgroups are significantly anisotropic, with a confidence of 9σ for α Sco, 3σ for β Sco, 3σ for δ Sco, 2σ for ν Sco, 4σ for π Sco, 4σ for ρ Oph, 3σ for σ Sco.

OB associations are typically sparse and unbound and thus are believed to be relatively dynamically unevolved (Wright 2020), i.e. they retain their initial velocity substructure, which is indicated by velocity anisotropy. The evidence of anisotropy in these subgroups indicates that they have not undergone sufficient dynamical mixing to develop isotropy and thus likely did not form as compact clusters.

5.2 Virial mass

In their analysis, Posch et al. (2025) estimate the masses of groups by multiplying the total number of likely members with the peak mass (0.42 $M_\odot$) of a Kroupa et al. (2001) IMF. Following this approach we estimate total masses of subgroups by taking the number of members of each from Miret-Roig et al. (2022b), apply a scaling factor which is the ratio of total YSOs per subgroup in our sample to new YSOs (those previously unallocated to subgroups by Miret-Roig et al. 2022b) and multiply by the peak mass. We approximate the uncertainty with a Poisson error. The approximate masses of subgroups are $\sim 480 \pm 16\,M_\odot$ for α Sco, $\sim 150 \pm 9\,M_\odot$ for β Sco, $\sim 310 \pm 13\,M_\odot$ for δ Sco, $\sim 110 \pm 8\,M_\odot$ for ν Sco, $\sim 330 \pm 12\,M_\odot$ for π Sco, $\sim 480 \pm 19\,M_\odot$ for ρ Oph and $\sim 560 \pm 19\,M_\odot$ for σ Sco (Table. 2). This then implies a total mass of $\sim 2420 \pm 96\,M_\odot$ for

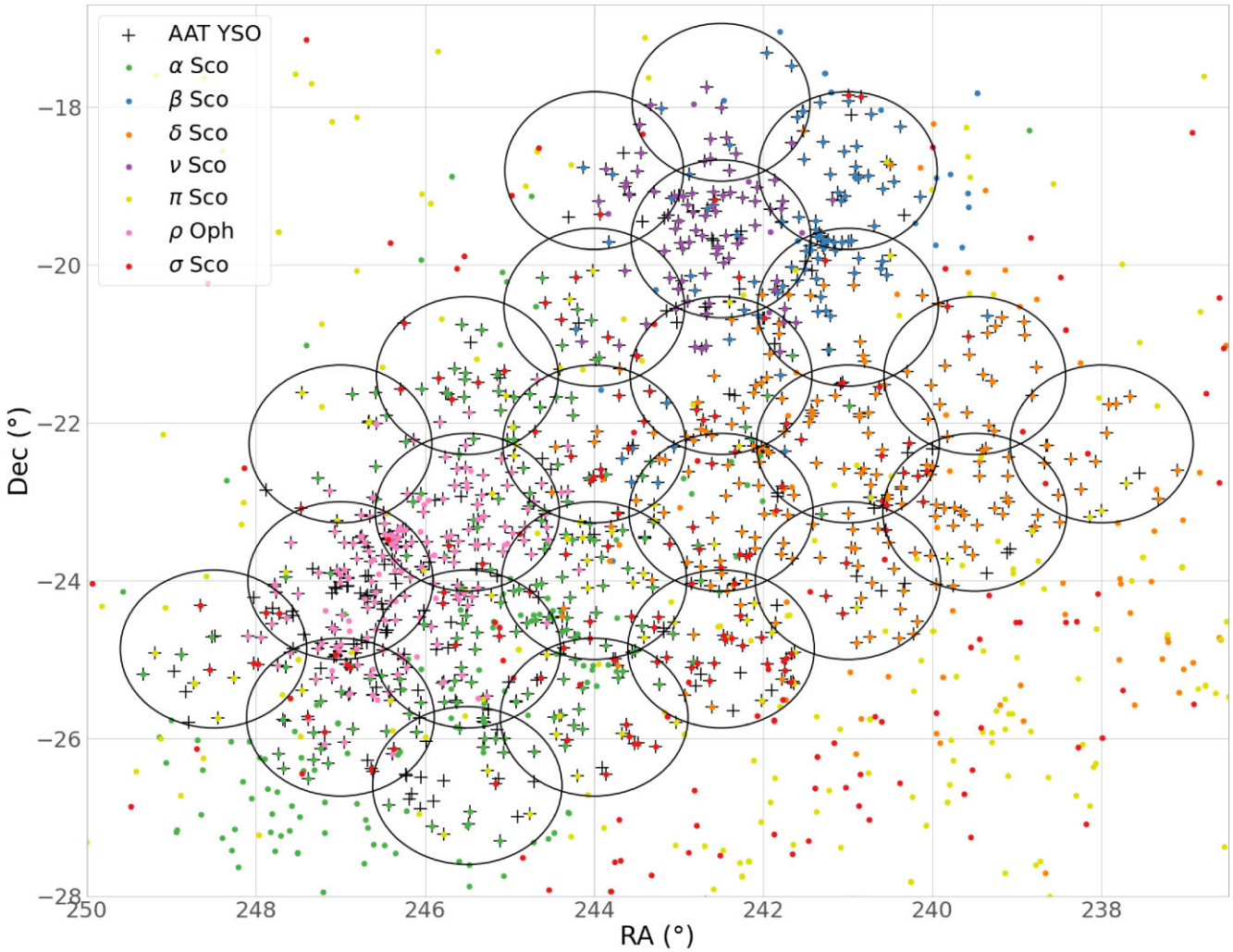

Figure 9. Sky positions of spectroscopically confirmed YSOs observed with the AAT, indicated with plus symbols, as well as the positions of Upper Sco subgroup members from Miret-Roig et al. (2022b) within the same magnitude range as our observed sample ($13 < G < 16.5$), colour-coded according to their subgroup membership. The 2°-diameter circles indicate the individual fields of observation of the AAT within which targets were selected.

Upper Sco, which is reasonable agreement with previous estimates ($\sim 2060\,M_\odot$; Preibisch & Mamajek 2008).

We combine our observed velocity dispersions to obtain 3D velocity dispersions (σ_{3D}) and using these we estimate virial masses for each subgroup according to

$$M_{\rm vir} = \eta \frac{\sigma_{3D}^2 r_{50}}{3G}, \quad (1)$$

where $\eta = 10$ (Zwart, McMillan & Gieles 2010), and r_{50} is the smallest radius containing half of a subgroup's member YSOs. These values are given in Table 2.

Our estimated virial masses for subgroups are all significantly larger than those estimated using the IMF, in some cases by an order of magnitude, which is evidence that these groups are gravitationally unbound. The lowest virial masses we obtain are for β Sco and ν Sco, the youngest subgroups after ρ Oph (Ratzenböck et al. 2023b), but even then their virial masses are twice and three times larger than their IMF-based mass estimates respectively. For subgroups with many candidate YSO members outside of the area covered by our observations (see Fig. 9), the half-mass radius r_{50} is likely underestimated, and thus so is our virial mass estimate.

The ρ Oph cluster in particular has previously been considered gravitationally bound (Rigliaco et al. 2016; Miret-Roig et al. 2022b; Wright et al. 2024) despite the large velocity dispersion among its member YSOs. In fact, our velocity dispersion in RVs for ρ Oph is in excellent agreement with the dispersion of Rigliaco et al. (2016) of $1.14 \pm 0.35\,{\rm km\,s^{-1}}$. This is due to the binding mass of gas still in the region, which has been estimated to be $\sim 1750\,M_\odot$ (Loren 1989), which well exceeds the virial mass we estimate.

5.3 Expansion velocity

We calculate expansion velocities $v_{\rm out}$ (${\rm km\,s^{-1}}$) similarly to Armstrong & Tan (2024), which are the components of velocity for each subgroup members directed away from the subgroup centre in 3D. The median $v_{\rm out}$ ($\bar{v}_{\rm out}$) and uncertainties for each subgroup are reported in Table 2. A significantly positive $\bar{v}_{\rm out}$ indicates overall expansion of the subgroup, while a significantly negative $\bar{v}_{\rm out}$ indicates overall contraction (Kuhn et al. 2019; Wright et al. 2024). We also count the number of subgroup members with positive individual expansion velocities and report the percentage per subgroup in Table 2.

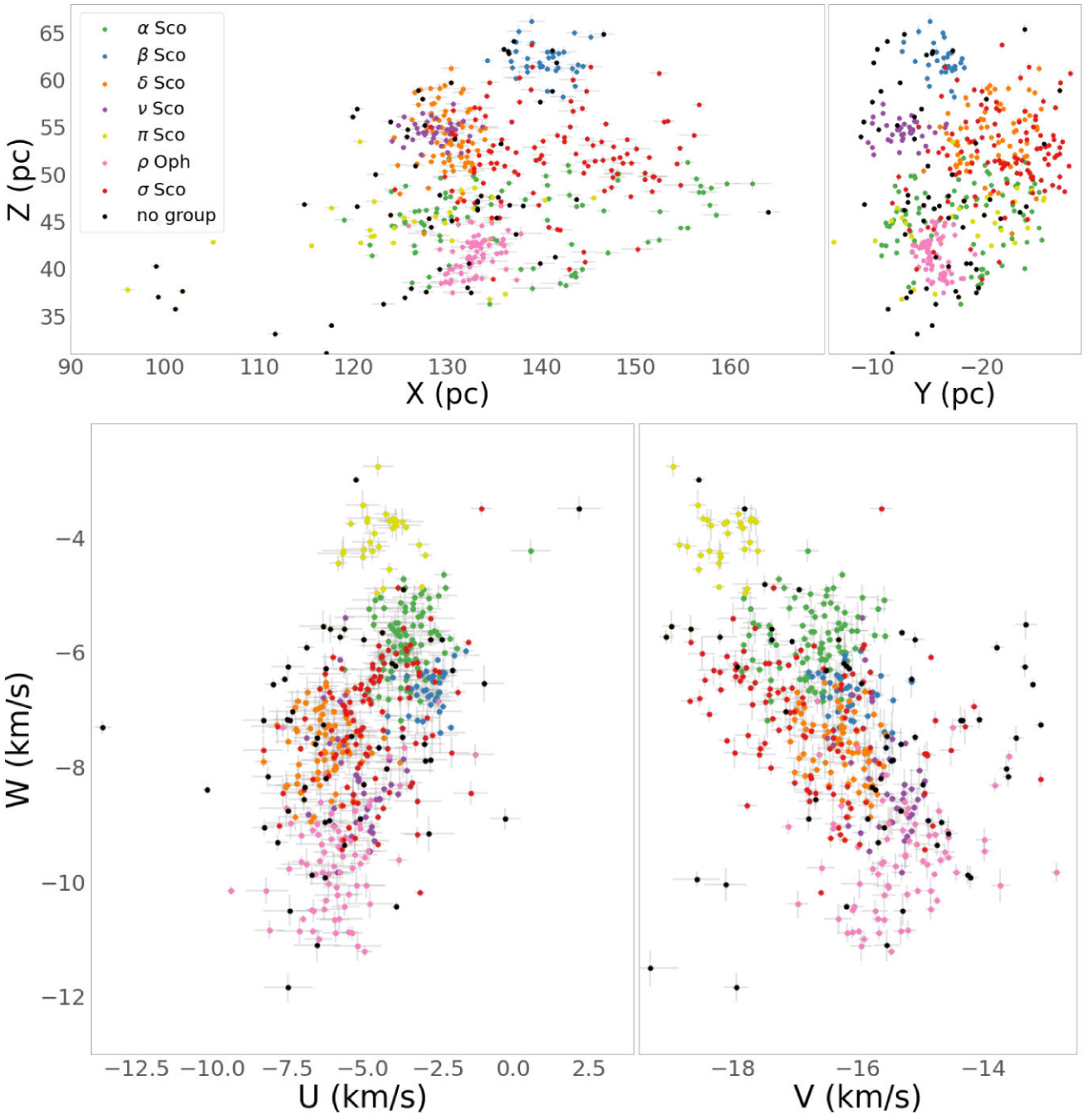

Figure 10. *Top:* Heliocentric Cartesian coordinates (XYZ) and *Bottom:* velocities (UVW) of confirmed YSOs coloured according to their kinematic groups.

For all subgroups, we find that $\bar{v}_{\rm out}$ is positive, though with varying significance. Also, all subgroups have at least 59 per cent of their members with 6D kinematic information moving away from the subgroup centre in 3D. The highest and also most significant $\bar{v}_{out}$ belongs to δ Sco ($\bar{v}_{out} = 0.46^{+0.05}_{-0.05}$ km s^{-1}), which is also the subgroup with the highest proportion of its members moving away from the subgroup centre (83 per cent). This is a reasonable value of $\bar{v}_{\rm out}$ for a young cluster, falling near the median of values found by Kuhn et al. (2019) and Wright et al. (2024).

Interestingly, the ρ Oph cluster, which has previously been considered gravitationally bound (Rigliaco et al. 2016; Miret-Roig et al. 2022b), has both a positive $\bar{v}_{\rm out}$ of $> 3.5\sigma$ significance and 72 per cent of its members have positive individual $v_{\rm out}$, which is evidence that this group is expanding despite the binding mass of gas in the region. Wright et al. (2024) calculated an expansion velocity of $\bar{v}_{out} = -0.34^{+0.01}_{-0.12}$ km s^{-1} for ρ Oph, implying contraction, though this was based on a sample of 38 member YSOs identified in the *Gaia*-ESO survey (Gilmore et al. 2022; Randich et al. 2022) within a $\sim 1^{\circ}$ diameter area centred on (RA $= 246.0^{\circ}$, Dec. $= -23.8^{\circ}$), whereas we have a sample of 162 YSOs with 6D kinematic information which are distributed across $\sim 4^{\circ}$. This discrepancy may indicate that there is a contracting core of YSOs in the centre of ρ Oph, surrounded by an expanding halo.

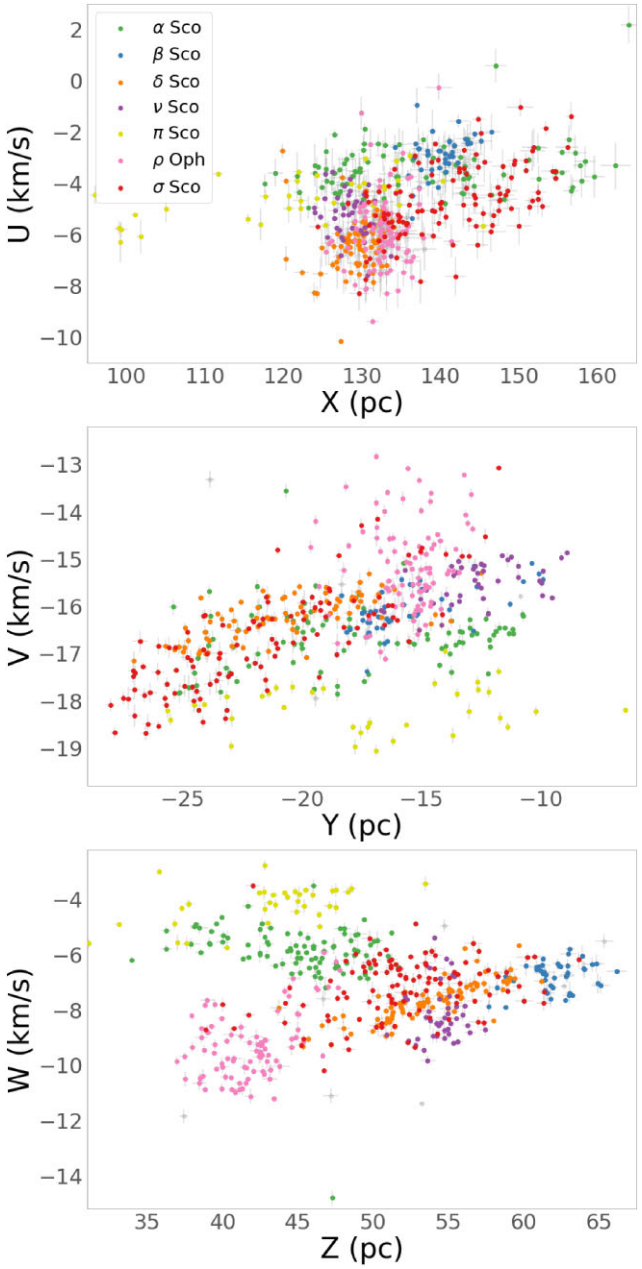

Figure 11. Heliocentric Cartesian coordinates (XYZ) and velocities (UVW) of confirmed YSOs coloured according to their kinematic groups.

However, simulations of young clusters (e.g. Sills et al. 2018; Kuhn et al. 2019) have indicated that bound clusters may still exhibit significantly positive median $v_{\rm out}$ up to ~ 0.5 km s^{-1} as they rebound from the initial collapse of hierarchical cluster assembly after ~ 1 Myr, until reaching an equilibrium at ~ 6 Myr. The ρ Oph cluster is within the age range (3–4 Myr; Ratzenböck et al. 2023b) when this rebound would be expected to happen, though it should be noted that Sills et al. (2018) simulated much more massive clusters ($> 1500\,M_\odot$) than ρ Oph is estimated to be ($\sim 480\,M_\odot$), which become nearly spherical after ~ 1 Myr following hierarchical cluster assembly, so it is unclear to what degree these simulations might represent the dynamical evolution of a sparser, low-mass cluster like ρ Oph.

5.4 Linear expansion trends

Linear expansion is a key indicator that a stellar association is unbound and in the process of dispersing into the Galactic field. The precise rates of expansion and potential anisotropy can also be useful in constraining an association's initial configuration and dynamical history.

We investigate evidence for expansion among the subgroups of Upper Sco by looking for linear correlations between Cartesian velocity and position in each direction, where positive or negative correlations will indicate either expansion or contraction, respectively. The best-fitting parameters for the linear correlations, the gradient, intersection and the fractional underestimation of the variance (m, b, f), are determined following the same approach as described in Armstrong et al. (2022), using Bayesian inference, with $> 3\sigma$ outliers in position and velocity removed. We also vary the positions of YSOs by randomly sampling from their uncertainties. We perform 2000 iterations with 200 walkers, half of which are discarded as burn in, and report the medians,16th and 84th percentiles from the posterior distribution as the linear best-fitting gradient and 1σ uncertainties respectively. Our results are listed in Table 3. In Fig. 14, we plot linear expansion trends for α Sco (green) and δ Sco (orange) as examples.

All groups show expansion trends of at least 3σ significance in at least one direction and β Sco, δ Sco, and σ Sco show trends of at least 3σ significance in all directions, but the direction of greatest expansion is not the same for all groups. α Sco, β Sco, and σ Sco show the greatest rate of expansion in the direction of Galactic rotation Y, whereas δ Sco, ν Sco, π Sco, and ρ Oph show the greatest rate of expansion in the direction perpendicular to the Galactic plane Z.

It is worth noting that the weak expansion trends in X may be due in part to the fact that this direction coincides most closely to the line-of-sight from the Sun, thus the errors on the X coordinate contain the largest component of parallax error, and the U velocity the largest component of RV error, including unresolved binarity, which remain the greatest sources of uncertainty in our 6D kinematic information.

In α Sco, δ Sco, and σ Sco, the rates of expansion are significantly anisotropic (at least 4σ). This anisotropy may indicate a level of kinematic substructure in these groups that has survived dynamical mixing. Despite the relatively old ages of these groups (Ratzenböck et al. 2023b; ~ 10 Myr;), they were likely formed too sparse to undergo significant mixing and will retain most of their substructure as they expand until they eventually disperse into the field, similar to what has been concluded for other nearby associations such as Vela OB2 (Wright 2020; Armstrong et al. 2022).

α Sco is the only subgroup to show evidence for contraction, at a rate of $-0.047^{+0.010}_{-0.010}$ km s^{-1} pc^{-1} in Z, the direction perpendicular to the Galactic plane.

We also fit linear gradients to the entire YSO sample, which are plotted in Fig. 17. We find significantly positive ($> 6\sigma$) linear expansion rates in all directions, of $0.053^{+0.007}_{-0.007}$ km s^{-1} in X versus U, $0.098^{+0.007}_{-0.008}$ km s^{-1} in Y versus V and $0.054^{+0.008}_{-0.008}$ km s^{-1} in Z versus W. This provides strong evidence that Upper Sco as a whole is unbound and expanding, with clear anisotropy ($> 4\sigma$ difference in expansion rates between X and Y). However, the expansion rates of the whole Upper Sco sample are distinct from any of the internal rates for subgroups given in Table. 3, which may indicate that the region-wide expansion trends are dominated by inter-subgroup kinematics rather than internal kinematics.

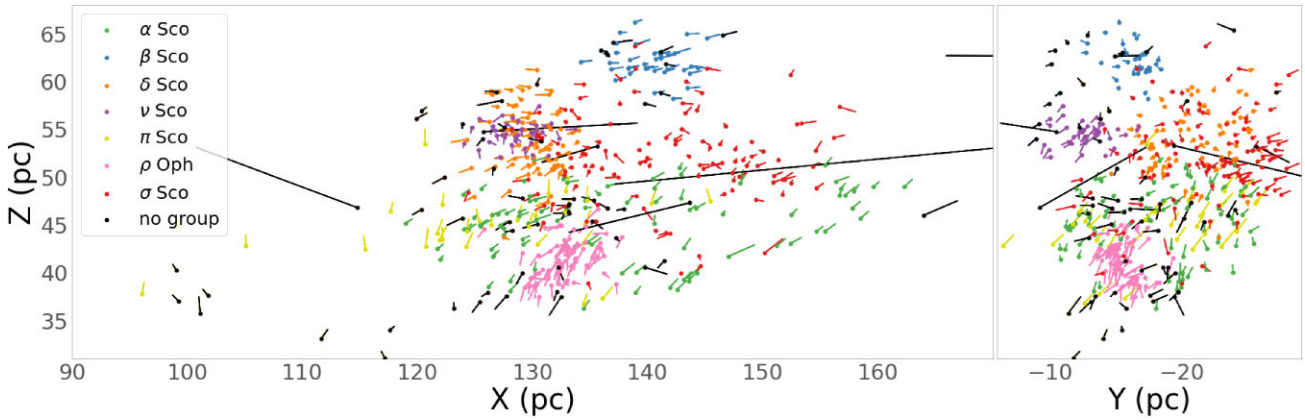

Figure 12. Heliocentric Cartesian coordinates of confirmed YSOs coloured according to their kinematic groups, with vectors indicating their velocities relative to the sample mean.

5.5 Expansion time-scales

We also derive expansion time-scales in Myr by inverting the greatest expansion rates of each subgroup, and list these results in Table 3. β Sco, δ Sco, ν Sco, ρ Oph, and σ Sco all yield expansion time-scales < 10 Myr, while α Sco and π Sco yield time-scales of $28.4^{+9.5}_{-5.7}$ and $16.0^{+5.8}_{-3.4}$ Myr, respectively, which are much larger than previous age estimates for these groups. On the other hand, the expansion time-scale of $6.2^{+0.4}_{-0.3}$ Myr for δ Sco agrees reasonably well with the kinematic ages of 4–6 Myr given in Miret-Roig et al. (2022b).

The expansion time-scales of $7.8^{+1.3}_{-0.9}$, $12.2^{+90.1}_{-5.7}$, $6.0^{+1.7}_{-1.1}$, and $5.0^{+0.5}_{-0.4}$ Myr for β Sco, ν Sco, ρ Oph, and σ Sco, respectively, are all significantly greater than the kinematic ages of 1–4, > 1, > 1, and 1–3 Myr given in Miret-Roig et al. (2022b) for these groups. In particular, Miret-Roig et al. (2022b) found no evidence that ρ Oph had been more compact in the past, and so estimated kinematic ages consistent with 0. However, since time-scales derived from expansion trends implicitly assume that the group of stars has been expanding from a point, they should be interpreted as upper limits. Therefore, there is no particular inconsistency between our expansion time-scales and these literature kinematic ages.

However, considering expansion time-scales as upper limit kinematic ages, it is then notable that both δ Sco and σ Sco in particular have expansion time-scales significantly lower than their isochronal age estimates, $9.8^{+1.2}_{-1.4}$ and $10.0^{+1.0}_{-0.5}$ Myr from Ratzenböck et al. (2023b), respectively. Such a difference between kinematic and isochronal ages has been hypothesized by Miret-Roig et al. (2024) to indicate a period in the early evolution of a cluster or association subgroup where the bulk of member YSOs remain gravitationally bound and possibly still embedded in their natal molecular cloud. The lower kinematic age then indicates when the subgroup becomes unbound and its members begin to disperse, possibly following residual gas expulsion. In the case of δ Sco and σ Sco, our expansion time-scales would imply embedded phases of $\sim$ 3–5 Myr, similar to the findings of Miret-Roig et al. (2024). However, the length of such a phase is highly uncertain as it depends on uncertainties in both kinematic and isochronal age methods. We discuss this further in Section 6.

5.6 Rotation

We also investigate evidence for rotation in the subgroups of Upper Sco by fitting linear gradients to combinations of velocity and position in different directions. Note that since these subgroups are gravitationally unbound these gradients may not indicate true rotation, but rather residual angular momentum. Our results are listed in Table 4. In Fig. 15, we plot linear rotation trends for ν Sco (purple) in X versus V and σ Sco (red) in X versus W as examples.

Rotation in young clusters has been hypothesized to arise from the merging of subclusters in the assembly phase of hierarchical cluster formation, the signature of which may even be stronger than that of cluster expansion in this scenario (e.g. Mapelli 2017). It is therefore a potential way of discriminating between hierarchical and monolithic cluster formation scenarios.

In the case of rotation found in substructures within an extended population such as an OB association, it may be inherited from the turbulent motion of the natal gas from which the substructure forms.

Significant ($> 3\sigma$) trends are found in at least one position–velocity pair in every subgroup. The subgroups with the greatest spatial extent (α, δ, and σ Sco) exhibit significant rotation trends in multiple directions, though, apart from a rotation rate of $-0.132^{+0.024}_{-0.024}$ km s^{-1}pc^{-1} in W versus Y for σ Sco, the rotation rates are relatively low in all directions in comparison to the expansion rates. These are among the older subgroups and so have had more time for expansion to suppress their rotation rates.

Meanwhile, ρ Oph, which is the densest and possibly youngest subgroup, exhibits the greatest rotation rates of $-0.133^{+0.038}_{-0.037}$ km s^{-1}pc^{-1} in U versus Z and of $-0.187^{+0.067}_{-0.062}$ km s^{-1} pc^{-1} in U versus Y. This is expected given that ρ Oph is still in a compact configuration and dynamically young, supporting the evidence from the asymmetry of its expansion trends (Section 5.4). That being said, these rates are still not significantly greater than the expansion rate in W versus Z, so there is not significant evidence for a hierarchical formation scenario for ρ Oph.

5.7 Traceback

With precise kinematic information, we can calculate the positions of stars in the past, and thus estimate when a cluster or association began expanding from its most initially compact configuration. This differs from a linear expansion age (Section 5.5) which, in effect, traces stars back to a point, and instead traces stars to an initial non-negligible volume.

We calculate 3D positions as a function of time following the same approach as Armstrong et al. (2022), using the epicycle approximation and the orbital equations from Fuchs et al. (2006), with the Oort A and B constants from Feast & Whitelock (1997),

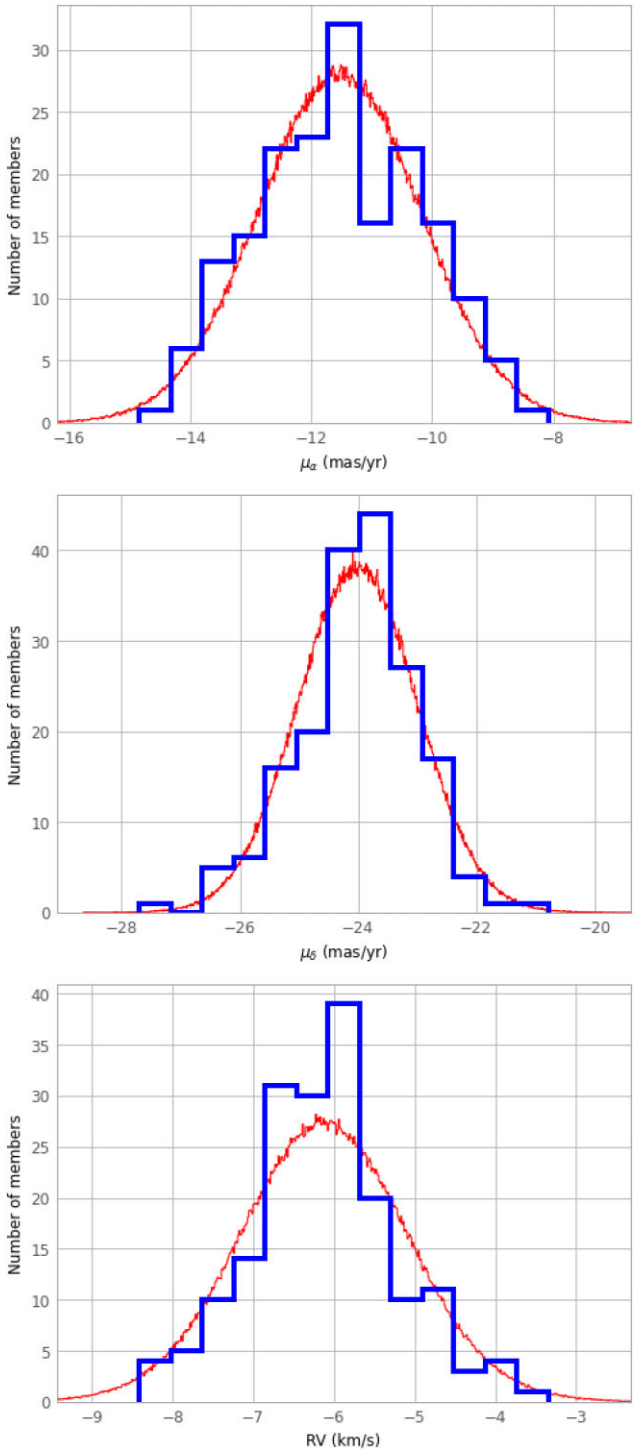

Figure 13. *Top:* Histogram of proper motion in RA for confirmed YSO members of δ Sco (blue), with MCMC best-fitting Gaussian distribution overplotted (red). *Middle:* Histogram of proper motion in Dec for confirmed YSO members of δ Sco (blue), with MCMC best-fitting Gaussian distribution overplotted (red). *Bottom:* Histogram of RVs for confirmed YSO members of δ Sco (blue), with MCMC best-fitting Gaussian distribution overplotted (red).

the local disc density from Holmberg & Flynn (2004), the local standard of rest velocity from Schönrich, Binney & Dehnen (2010) and a solar Z distance above the Galactic plane of 17 pc (Karim & Mamajek 2017). 3D positions are calculated up to 10 Myr in the past in 0.1 Myr steps. At each step, we calculate the spatial coherence of the association using both the total length of the minimum spanning tree (MST) between YSO members of a subgroup (Squicciarini et al. 2021), which we denote as $\tau_{\rm MSTlength}$, and the sum of 3D distances between YSOs and the median position of the subgroup (Quintana & Wright 2022), which we denote as $\tau_{\rm DSum}$. We estimate uncertainties on these using a Monte Carlo process with 1000 iterations, taking the 84th and 16th percentiles of the posterior distribution as the 1σ uncertainties. We plot the resulting metrics as functions of traceback time t in Fig. 16 with different filters on the cluster members included, all members in red, 3σ velocity outliers removed in green, 2σ velocity outliers removed in blue, and the 32 per cent longest branches removed in black (Fig. 16 *left*). We also give the traceback times at which these metrics are minimized, with uncertainties, in Table 2.

For $\tau_{\rm MSTlength}$ and $\tau_{\rm DSum}$, negative values indicate that a subgroup would have been at its most compact in the past, while positive values indicate that a subgroup will be more compact in the future. Both α Sco and ν Sco, which exhibited evidence for contraction in Table 3, have positive $\tau_{\rm MSTlength}$ and $\tau_{\rm DSum}$ values, and are thus likely to become more compact in the future, while the other groups are likely to have been more compact in the past.

$\tau_{\rm MSTlength}$ and $\tau_{\rm DSum}$ estimates for each of β Sco, δ Sco, ρ Oph, and σ Sco of $-0.4^{+0.4}_{-0.5}$ and $-1.0^{+0.5}_{-0.4}$ Myr, $-2.3^{+0.4}_{-0.5}$ and $-2.3^{+0.3}_{-0.3}$ Myr, $-0.7^{+0.4}_{-0.3}$ and $-0.5^{+0.2}_{-0.2}$ Myr, $-1.9^{+0.3}_{-0.3}$ and $-2.3^{+0.5}_{-0.4}$ Myr, respectively, are consistent between size metrics. However, the $\tau_{\rm MSTlength}$ and $\tau_{\rm DSum}$ estimates for π Sco of $0.1^{+0.5}_{-0.5}$ and $-4.2^{+0.8}_{-0.8}$ Myr are significantly different, as are estimates for α Sco of $0.4^{+0.5}_{-0.6}$ and $1.8^{+0.2}_{-0.4}$ Myr. This possibly indicates a certain amount of substructure remaining within these subgroups, making these different size metric inconsistent. Notably, these two subgroups are not recovered by the SIGMA algorithm (Ratzenböck et al. 2023b) in the same forms as by Miret-Roig et al. (2022b) with HDBSCAN, but their members are redistributed primarily among the Antares, ρ Sco and US-foreground populations.

Miret-Roig et al. (2022b) estimated dynamical traceback ages for these groups using a similar approach to ours, but used the determinant and trace of a covariance matrix consisting of radial, azimuthal, and vertical sizes as the metrics minimized to determine the most compact configuration of groups in the past. According to the trace of the covariance matrix the subgroups have dynamical ages of, 1.0 ± 1.2 Myr (α Sco), 2.5 ± 1.6 Myr (β Sco), 4.6 ± 1.1 Myr (δ Sco), 0.3 ± 0.5 Myr (ν Sco), 6.3 ± 1.4 Myr (π Sco), 0.0 ± 0.3 Myr (ρ Oph), and 2.1 ± 0.7 Myr (σ Sco). While our dynamical age estimates $\tau_{\rm MSTlength}$ and $\tau_{\rm DSum}$ agree well with those of Miret-Roig et al. (2022b) for σ Sco and within uncertainties for ν Sco, they are notably different for the majority of subgroups. For α Sco, β Sco, δ Sco, and π Sco we obtain younger dynamical ages than Miret-Roig et al. (2022b) according to both of our size metrics, while for ρ Oph we find larger dynamical ages according to both metrics.

The most likely causes of this difference in dynamical ages are the difference in samples of subgroup members and RVs available to enable dynamical traceback in 3D. The fact that we obtain younger dynamical ages for the majority of subgroups indicates that they may have become gravitationally unbound more recently than previously suggested.

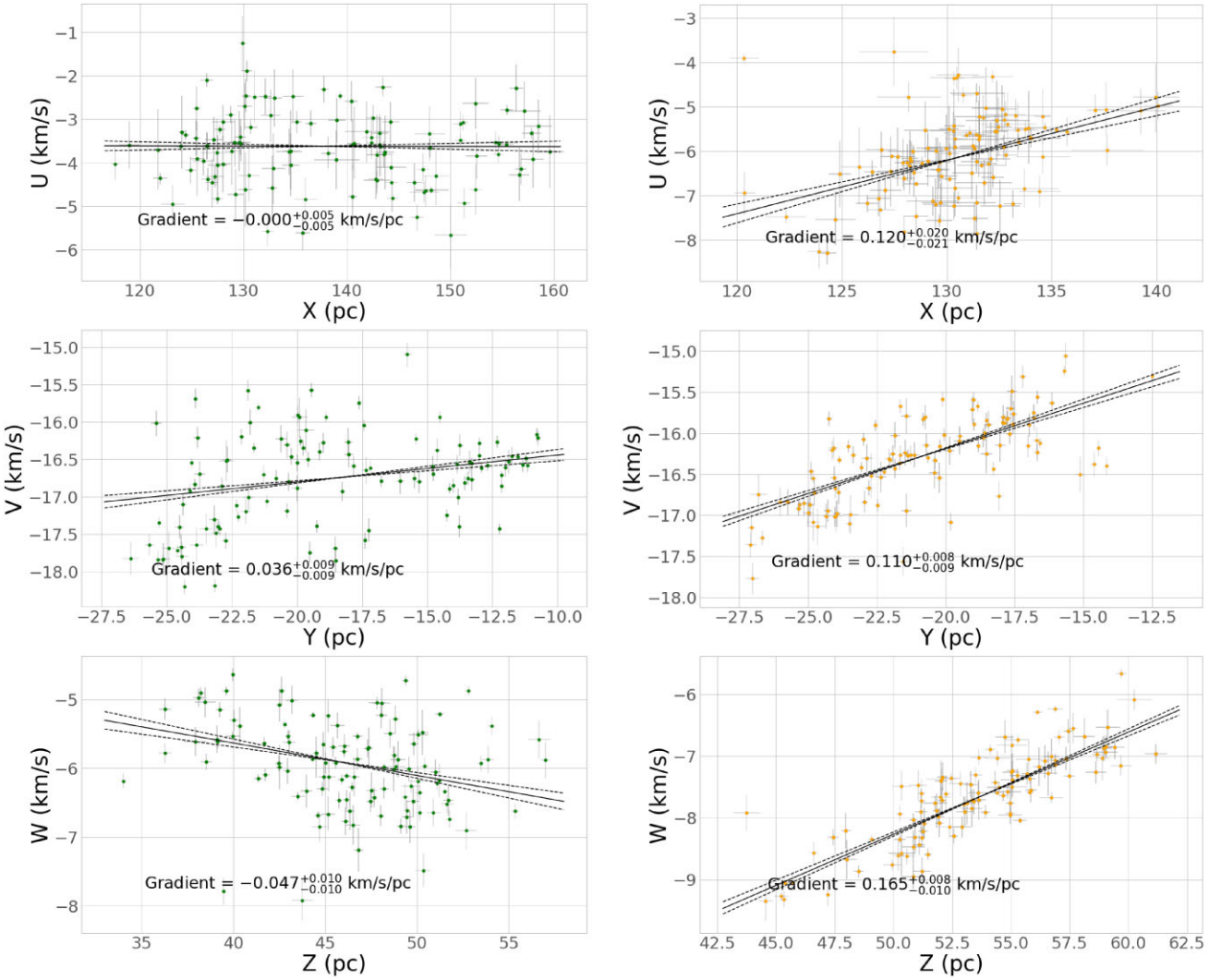

Figure 14. Cartesian velocity versus position in each of the three dimensions XYZ for stars in α Sco (green) and δ Sco (orange) with uncertainties shown. The best-fitting gradients and the 16th and 84th percentiles values of the fit are shown as solid and dashed lines respectively in each panel.

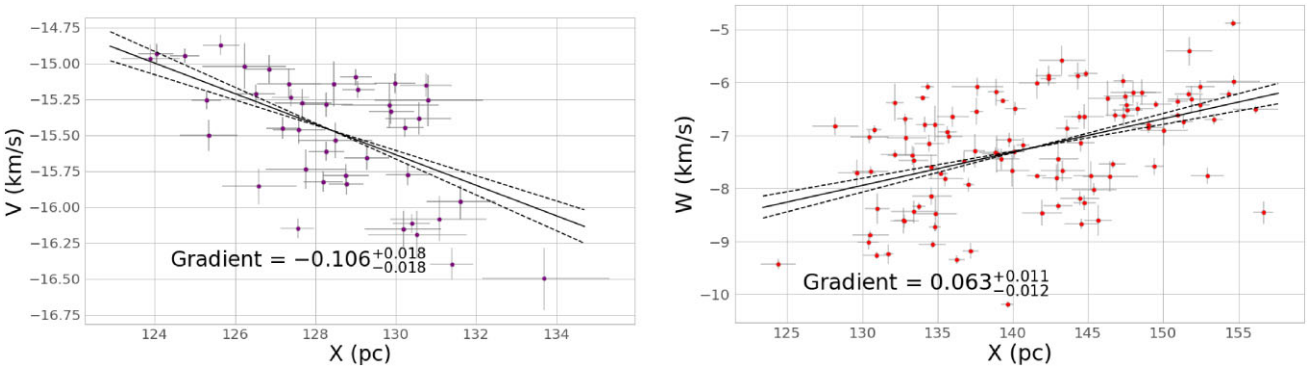

Figure 15. Cartesian V velocity versus X position for stars in ν Sco (purple) and W versus X for stars in σ Sco (red) with uncertainties shown. The best-fitting gradients and the 16th and 84th percentiles values of the fit are shown as solid and dashed lines respectively in each panel.

5.7.1 Initial size

We also estimate the initial size of each subgroup via several metrics. We calculate half-mass radii and the radii containing 90 per cent of subgroup members at the times when they were most compact, $r_{50}(\tau_0)$ and $r_{90}(\tau_0)$, according to the dynamical ages $\tau_{\rm MSTlength}$ and $\tau_{\rm DSum}$. These radii are given in Table 2. It should be noted that since α and ν Sco have positive dynamical ages, we do not expect their initial configurations to be significantly more compact than the present day distributions.

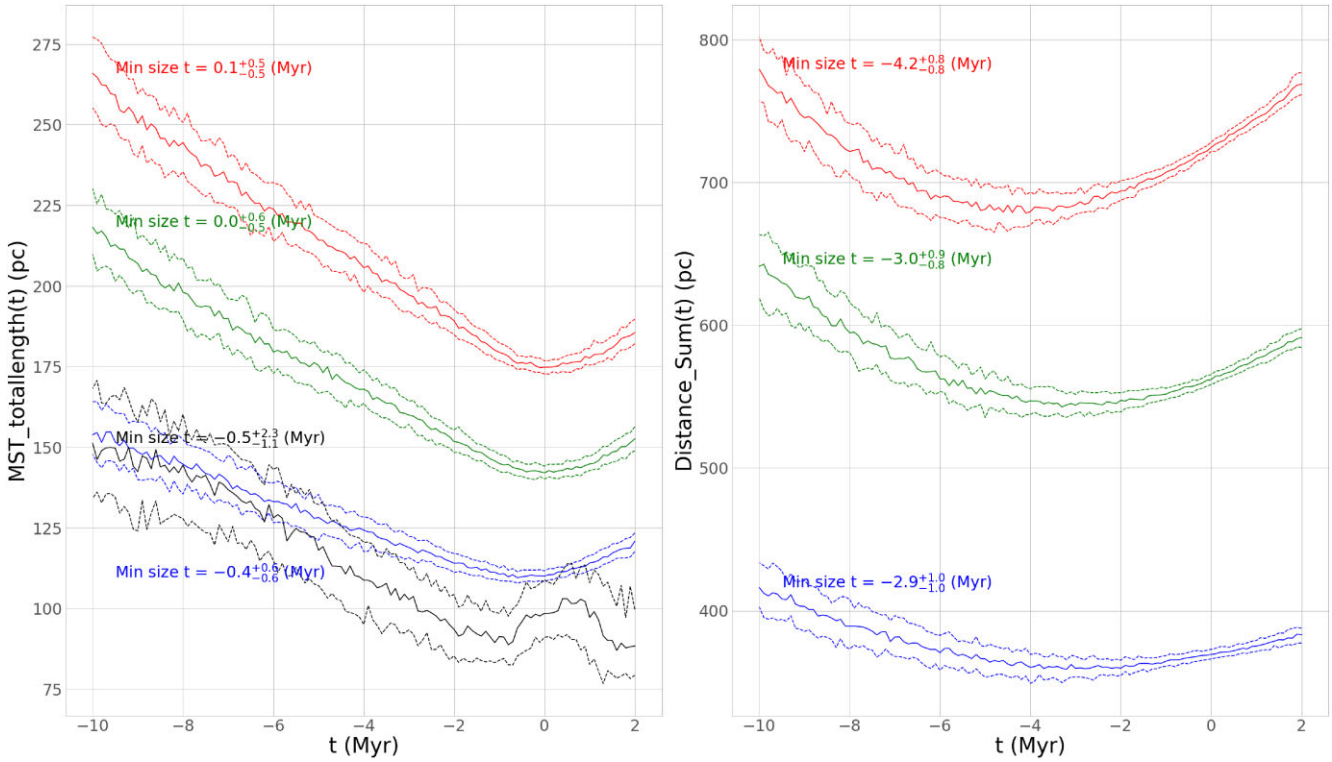

Figure 16. *Left:* Minimum spanning-tree total length as a function of trace-back time with no filter for outliers (red), 3σ velocity outliers removed (green), 2σ velocity outliers removed (blue) and 32 per cent longest branches removed (black) with their respective uncertainties. *Right:* Sum of distances for each star to the association subgroup centre as a function of trace-back time with no filter for outliers (red), 3σ velocity outliers removed (green), 2σ velocity outliers removed (blue). This example illustrates the traceback of the π Sco subgroup.

Cometary or pillar shaped cloud structures within which protostars are thought to form from triggering via feedback, such as the 'Pillars of Creation' in the Eagle Nebula, have been observed to have typical diameters ~ 1 pc (e.g. Miao et al. 2006). If the subgroups of Upper Sco had formed in such structures, as has been proposed in the 'cluster-chain' triggered formation scenario (Posch et al. 2025), we would expect their initial sizes to be similar. However, we find that even the subgroups which become most compact at their initial configurations have half-mass radii $r_{50}(\tau_0) > 2.5$ pc and 90 per cent radii $r_{90}(\tau_0) > 4.5$ pc, an order of magnitude larger than such pillar structures.

However, this estimate of initial size will be inflated by scatter due to observational uncertainties in parallax, proper motions and RVs which are propagated through the traceback calculation. We estimate the inflation of the radii $r_{50}(\tau_0)$ and $r_{90}(\tau_0)$ due to uncertainties by performing numerical simulations, where we create a synthetic population of n stars equal to the number of confirmed YSOs with 6D kinematics per subgroup in our data, and place them at the origin of a 3D Cartesian space. We then add perturbations in 3D positions and velocities randomly sampled from the observed position and velocity uncertainties to the synthetic population of stars and calculate their radial distances from the origin at time t, equal to the larger of the dynamical traceback ages $\tau_{\rm MSTlength}$ or $\tau_{\rm DSum}$ for a given subgroup. We then calculate the radii $r_{50}(\tau_0)$ and $r_{90}(\tau_0)$ of the synthetic populations at time t. We perform 10 000 iterations of this simulation for each subgroup and take the median of the posterior distributions of $r_{50}(\tau_0)$ and $r_{90}(\tau_0)$ as the predicted inflation of initial size estimates, and the 16th and 84th percentiles values as the 1σ uncertainties.

For the subgroups hypothesized to belong to the 'cluster-chains' described by (Posch et al. 2025) which we infer to have been more compact in the past via our traceback calculations (β Sco, δ Sco, ρ Oph, and σ Sco), we estimate that $r_{50}(\tau_0)$ for β Sco is inflated by $1.26^{+0.10}_{-0.10}$ pc, $r_{90}(\tau_0)$ for β Sco is inflated by $2.47^{+0.21}_{-0.20}$ pc, $r_{50}(\tau_0)$ for δ Sco is inflated by $0.42^{+0.02}_{-0.02}$ pc, $r_{90}(\tau_0)$ for δ Sco is inflated by $0.80^{+0.04}_{-0.04}$ pc, $r_{50}(\tau_0)$ for ρ Oph is inflated by $0.56^{+0.04}_{-0.04}$ pc, $r_{90}(\tau_0)$ for ρ Oph is inflated by $1.22^{+0.09}_{-0.08}$ pc, $r_{50}(\tau_0)$ for σ Sco is inflated by $2.03^{+0.15}_{-0.14}$ pc and $r_{90}(\tau_0)$ for σ Sco is inflated by $4.04^{+0.31}_{-0.29}$ pc.

In each of these cases, the estimated initial sizes of these subgroups can not be accounted for by scatter due to observational uncertainties alone. Subtracting the estimates of inflation from the estimated radii for these subgroups still results in $r_{50}(\tau_0) > 2.0$ pc and $r_{90}(\tau_0) > 4.0$ pc.

We acknowledge the caveat that we are not accounting for unresolved binaries in our sample when making these estimates, which we would expect to contribute to scatter in the RVs especially. With further information about binarity among YSOs, more complete coverage of the region with spectroscopic observations for RVs and youth identification, and with greater precision of parallaxes and proper motions with the upcoming *Gaia* DR4, improved estimates of the initial size of subgroups in Upper Sco could provide strong constraints on the likely star formation scenario of the region.

5.8 Intergroup kinematics

As well as the internal kinematics of each separate subgroup, we can also consider the kinematic trends between subgroups.

We calculate the component of 3D velocity directed away from the combined centre of Upper Sco ($v_{\rm out}$) for each subgroup, using

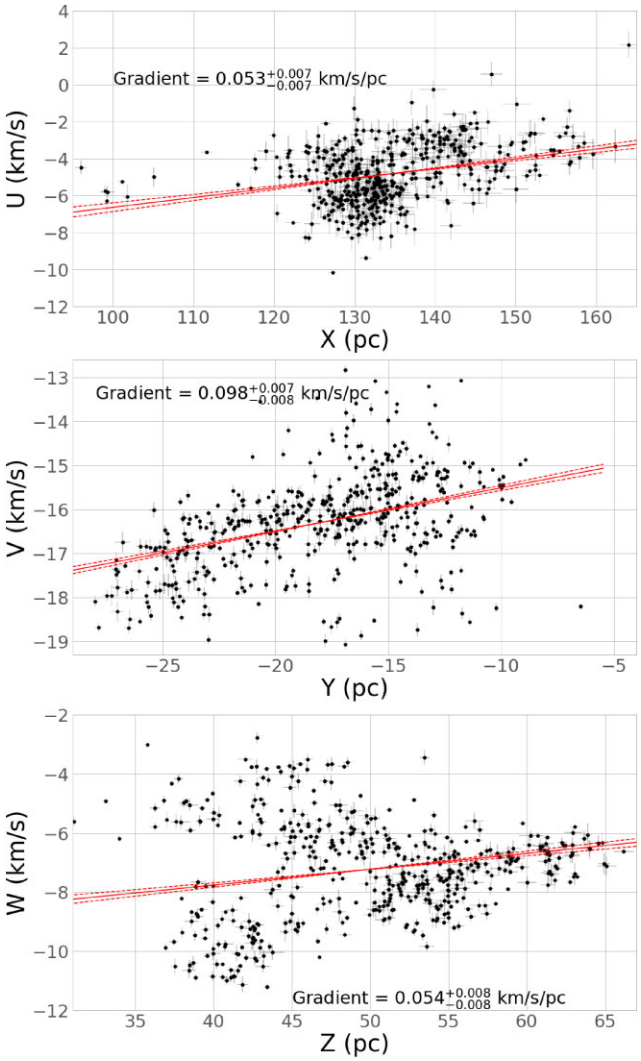

Figure 17. Cartesian velocity versus position in each of the three dimensions XYZ for all YSOs in our sample with uncertainties shown. The best-fitting gradients and the 16th and 84th percentiles values of the fit are shown as red solid and dashed lines respectively in each panel.

the median subgroup Cartesian positions and velocities and their respective uncertainties as given in Table. 2, and using the median Cartesian position and velocity of all YSOs in our sample as the combined centre of Upper Sco.

We find $v_{\rm out} = -1.26^{+0.04}_{-0.04}$ km s^{-1} for α Sco, $v_{\rm out} = 1.95^{+0.11}_{-0.11}$ km s^{-1} for β Sco, $v_{\rm out} = -0.54^{+0.03}_{-0.03}$ km s^{-1} for δ Sco, $v_{\rm out} = -0.31^{+0.04}_{-0.04}$ km s^{-1} for ν Sco, $v_{\rm out} = 0.56^{+0.14}_{-0.14}$ km s^{-1} for π Sco, $v_{\rm out} = 1.60^{+3.00}_{-0.15}$ km s^{-1} for ρ Oph, and $v_{\rm out} = 0.36^{+0.12}_{-0.12}$ km s^{-1} for σ Sco.

Despite the evidence we have presented that most of these subgroups are expanding from their initial configurations, albeit anisotropically (see Section 5.4), we find that the large-scale motions of Upper Sco are not consistent with simple radial expansion of all subgroups relative to one another. Indeed, α Sco, δ Sco, and ν Sco are moving toward the combined centre of Upper Sco on average, as indicated by their significantly ($> 7\sigma$ in all cases) negative $v_{\rm out}$ values.

We also calculate the intersubgroup velocity dispersion, again using the median velocities of each subgroup as given in Table. 2. The inter-subgroup velocity dispersion in the X direction (σ_U) = $1.09^{+0.03}_{-0.03}$ km s^{-1}, in the Y direction (σ_V) = $0.89^{+0.01}_{-0.01}$ km s^{-1} and in the Z direction (σ_W) = $1.66^{+0.01}_{-0.01}$ km s^{-1}.

If we calculate the intersubgroup velocity dispersions with the velocity components attributed to radial expansion ($v_{\rm out}$) subtracted, we find $\sigma_U = 0.26^{+0.04}_{-0.04}$ km s^{-1}, $\sigma_V = 0.62^{+0.02}_{-0.02}$ km s^{-1}, and $\sigma_W = 1.01^{+0.04}_{-0.04}$ km s^{-1}.

We also note that, despite the significant expansion trends seen across the entire Upper Sco YSO sample (Fig. 17) the greatest of which ($0.098^{+0.007}_{-0.008}$ km s^{-1} pc^{-1}) indicates an expansion time-scale of $10.20^{+0.91}_{-0.68}$ Myr, traceback calculations performed for the entire sample following the approach described in Section. 5.7 do not provide strong evidence that the region as a whole was significantly more compact in the past (Fig. 18). According to the $\tau_{\rm MSTlength}$ size metric the distribution of Upper Sco YSOs becomes sparser back in time, with the minimum MST total-length being found consistently in the present configuration, regardless of the level of filtering. According to the $\tau_{\rm DSum}$ metric the distribution of Upper Sco YSOs may be considered to be more compact $\sim$ 1.1–1.6 Myr in the past, but then becomes sparser for earlier times (Fig. 18). We also plot the relative positions of all YSOs in our sample at the present time, at 1.6 Myr in the past and at 3.2 Myr in the past in Fig. 19 as a visualization of this traceback.

A possible reason for this difference may be the sensitivity of the traceback to minimum configuration approach to kinematic outliers and, in this case, a potential interloper subgroup. The large negative $v_{\rm out}$ of α Sco, as well as its older isochronal age relative to most other subgroups, indicates its likely origin outside of Upper Sco as it is commonly defined, or at least that its formation was not directly related to the subgroups considered part of the Upper Sco 'cluster-chain' by Posch et al. (2025). This is similar to the conclusion of Armstrong et al. (2022) that the NGC 2547 cluster is presently interloping in the younger population of Vela OB2. The linear expansion analysis is less sensitive to kinematic outliers and so still produces significant expansion gradients for Upper Sco as a whole despite the inclusion of α Sco.

If the traceback calculations are performed on the YSOs sample with α Sco removed, then the traceback time to the most compact configuration becomes $2.4^{+0.2}_{-0.2}$, $3.0^{+0.2}_{-0.3}$, and $2.3^{+0.3}_{-0.3}$ Myr, according to the $\tau_{\rm DSum}$ metric with no filter for outliers, 3σ velocity outliers removed and 2σ velocity outliers removed, respectively.

6 DISCUSSION

6.1 Association membership

The confirmation of 1204 YSOs in the Upper Scorpius region, 118 that were not included in the clustering of Miret-Roig et al. (2022b), and 62 YSOs not included in Ratzenböck et al. (2023b), underlines the importance of spectroscopic indicators for accurate identification of members of young associations with complex kinematics.

There are also 35 members of the Miret-Roig et al. (2022b) clusters in our sample that we cannot confirm as YSOs via either spectroscopic indicators or *Gaia* variability. Five of these have AAT-HERMES spectra of $SNR > 20$, and so are unlikely to be YSOs, while the others have $SNR < 5$ and so may not be confirmed due to large uncertainties in measured EW(Li).

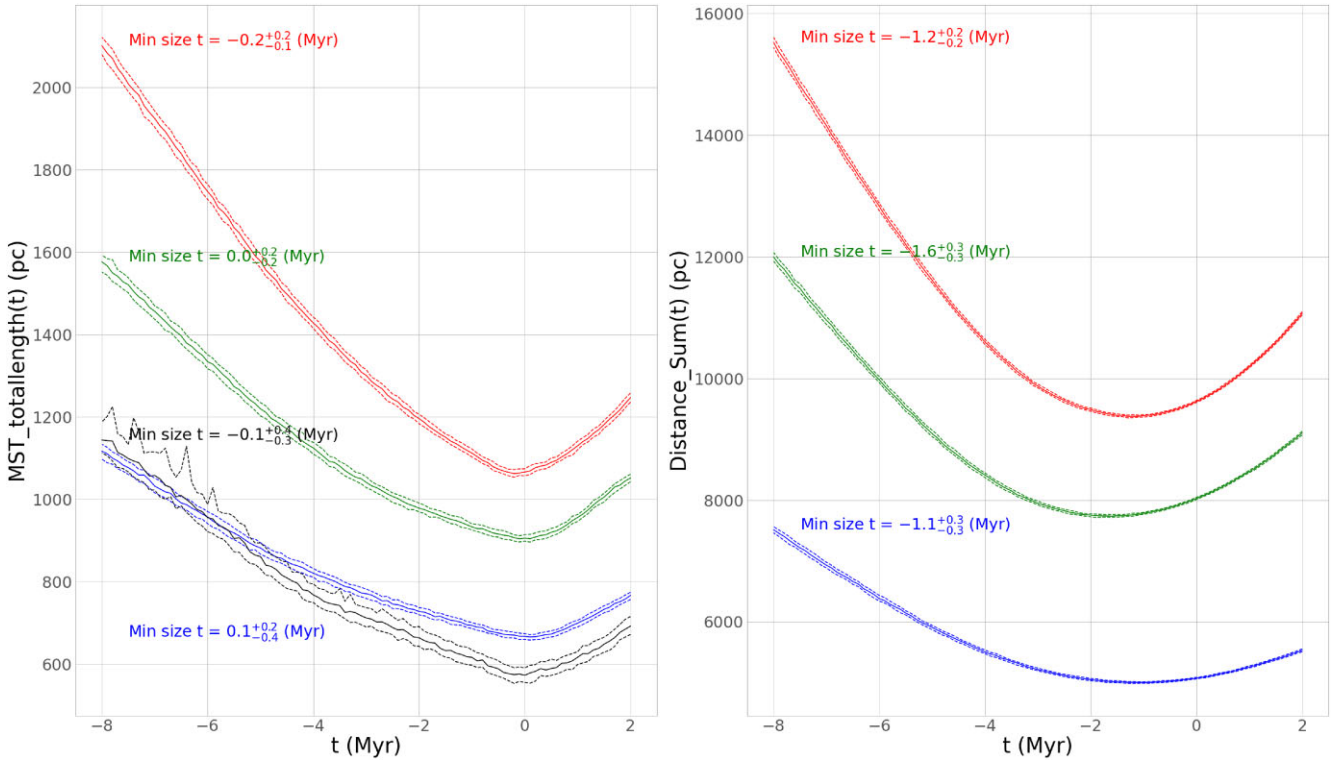

Figure 18. Association size for all YSOs with quality 6D kinematic information in our Upper Sco sample. *Left:* Minimum spanning-tree total length as a function of trace-back time with no filter for outliers (red), 3σ velocity outliers removed (green), 2σ velocity outliers removed (blue) and 32 per cent longest branches removed (black) with their respective uncertainties. *Right:* Sum of distances for each star to the association subgroup centre as a function of trace-back time with no filter for outliers (red), 3σ velocity outliers removed (green), 2σ velocity outliers removed (blue).

6.2 The likely star formation scenario of the Upper Scorpius association

Fig. 20 presents a summary of the spatial distribution and kinematics that we have derived for the sub-groups of the Upper Sco OB association. Previous studies of this region have found evidence of an age gradient among the different subgroups present (Squicciarini et al. 2021; Ratzenböck et al. 2023b), and thus infer scenarios of sequential star formation in this region. In particular, Posch et al. (2023, 2025) recently proposed a star formation scenario in which feedback from massive stars in the oldest subgroups compresses molecular gas in an adjacent region, initiating a new generation of star formation while simultaneously pushing the star-forming gas away, similar to the triggered formation scenario of Elmegreen & Lada (1977). They invoke this scenario as an explanation for both the age gradient found in Upper Sco, with the older groups δ Sco and σ Sco being centrally located and younger groups such as ν Sco being located toward the periphery of Upper Sco, as well as the apparent outward acceleration of the younger groups relative to the older groups. In this 'cluster-chain' scenario, δ Sco and σ Sco are proposed to have triggered star formation in β Sco, which subsequently triggered the formation of ν Sco.

Our dynamical ages are generally younger than, and have a smaller range than, those of Miret-Roig et al. (2022b), which does not necessarily indicate that the groups are younger, but rather that they began expanding (i.e. became free of gas or unbound) more recently than previously suggested (Miret-Roig et al. 2024).

In the case that residual gas expulsion is the mechanism by which these groups became unbound and initiated expansion, one would assume that feedback should expel gas within the cluster (and thus cause unbinding of the subgroup) before triggering star formation at a more distant region of the molecular cloud. Then the smaller differences between dynamical ages of these groups also indicates shorter intervals between subgroup formation for the triggering via feedback to occur.

In fact, such a scenario requires that the unbinding of the first cluster ($C1$) precedes the formation of the second in the sequence ($C2$). Thus, assuming that an accurate isochronal cluster age ($\tau_{\rm iso}$) indicates the formation time of a cluster and a dynamical age ($\tau_{\rm dyn}$) indicates the time of unbinding, sequential cluster formation requires that

$$\tau_{{\rm dyn},C1} > \tau_{{\rm iso},C2}. \quad (2)$$

In the case of the proposed cluster chain δ Sco $\rightarrow$ β Sco $\rightarrow$ ν Sco (Posch et al. 2025), isochronal ages are estimated to be $9.8^{+1.2}_{-1.4}$, $7.6^{+0.8}_{-0.7}$, and $5.8^{+1.8}_{-0.5}$ Myr, respectively (Ratzenböck et al. 2023b, according to PARSEC models with BP–RP colour), but have dynamical ages of $2.3^{+0.3}_{-0.3}$, $1.0^{+0.4}_{-0.4}$, and $-0.1^{+0.3}_{-0.3}$ Myr, respectively by our estimation of $\tau_{\rm DSum}$, and dynamical ages of $4.6^{+0.6}_{-0.6}$, $2.4^{+1.7}_{-1.7}$, and $0.3^{+0.5}_{-0.5}$ Myr, respectively according to Miret-Roig et al. (2024). Notably, the oldest dynamical age of a cluster in this chain (δ Sco) is less than the lowest isochronal age (ν Sco), indicating that no cluster in this proposed chain had expelled its surrounding gas and become unbound until star formation had already begun in all the other clusters. This brings into doubt a scenario where the star formation of the younger groups was triggered by feedback from the previous group in a chain.

A possible alternative explanation that preserves the sequential cluster-chain hypothesis is that the clusters do not become unbound immediately after gas expulsion and before triggering the formation

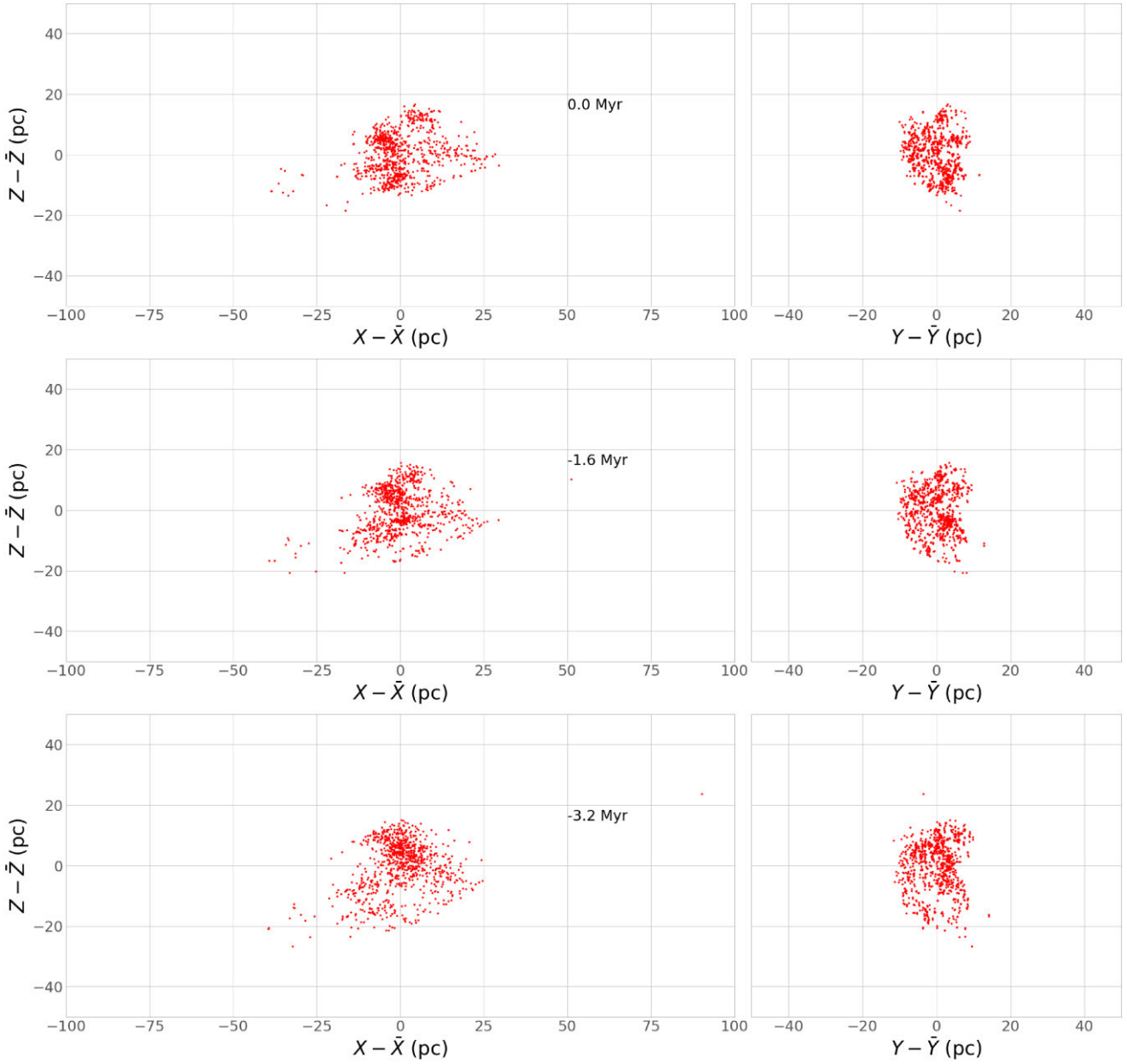

Figure 19. Relative Cartesian positions for all YSOs with quality 6D kinematic information in our sample at the present, 1.6 Myr in the past and 3.2 Myr in the past.

of the next cluster in the sequence, but several Myr later via a different mechanism, perhaps from gradual mass-loss as unbound stars escape or from tidal forces exerted by nearby molecular clouds. Thus $\tau_{\mathrm{dyn},C1} > \tau_{\mathrm{iso},C2}$ would no longer be required. However, in this case the dynamical age does not indicate when a cluster became gas free, and so the difference between isochronal ages and dynamical ages does not give us the time-scale of an 'embedded phase' as suggested by Miret-Roig et al. (2024).

This seems unlikely though, given that natal molecular gas makes up a significant proportion of an embedded cluster's binding mass, and so the infant mortality rate of clusters having undergone residual gas expulsion is expected to be at least 50 per cent (e.g. Goodwin & Bastian 2006). (Wright et al. 2024) found that the clusters they studied were all gravitationally unbound when considering the stellar mass only, but were nearly all gravitationally bound when considering the gas and stellar mass. This is very strong evidence for residual gas expulsion being responsible for unbinding a cluster. Our traceback analysis of the subgroups of Upper Sco indicates that they were likely initially too sparse, as well as too low-mass, to survive gas expulsion. Thus we consider that the dynamical age likely does indicate when gas expulsion occurred for each subgroup.

The anisotropy of velocity dispersions (Table 2) and expansion rates (Table 3), as well as the low fractions of subgroup members consistent with moving away from their subgroup centre in 3D (Table 2), indicate that subgroups did not expand uniformly from initially compact configurations, but rather formed with significant kinematic substructure. The initial size estimates we make for subgroups (Section 5.7.1) as well as the short dynamical ages relative to linear expansion rates ($1.0^{+0.4}_{-0.4}$ and $7.81^{+1.32}_{-0.94}$ Myr, respectively for β Sco, $-0.1^{+0.3}_{-0.3}$ and $12.18^{+90.12}_{-5.66}$ Myr, respectively for

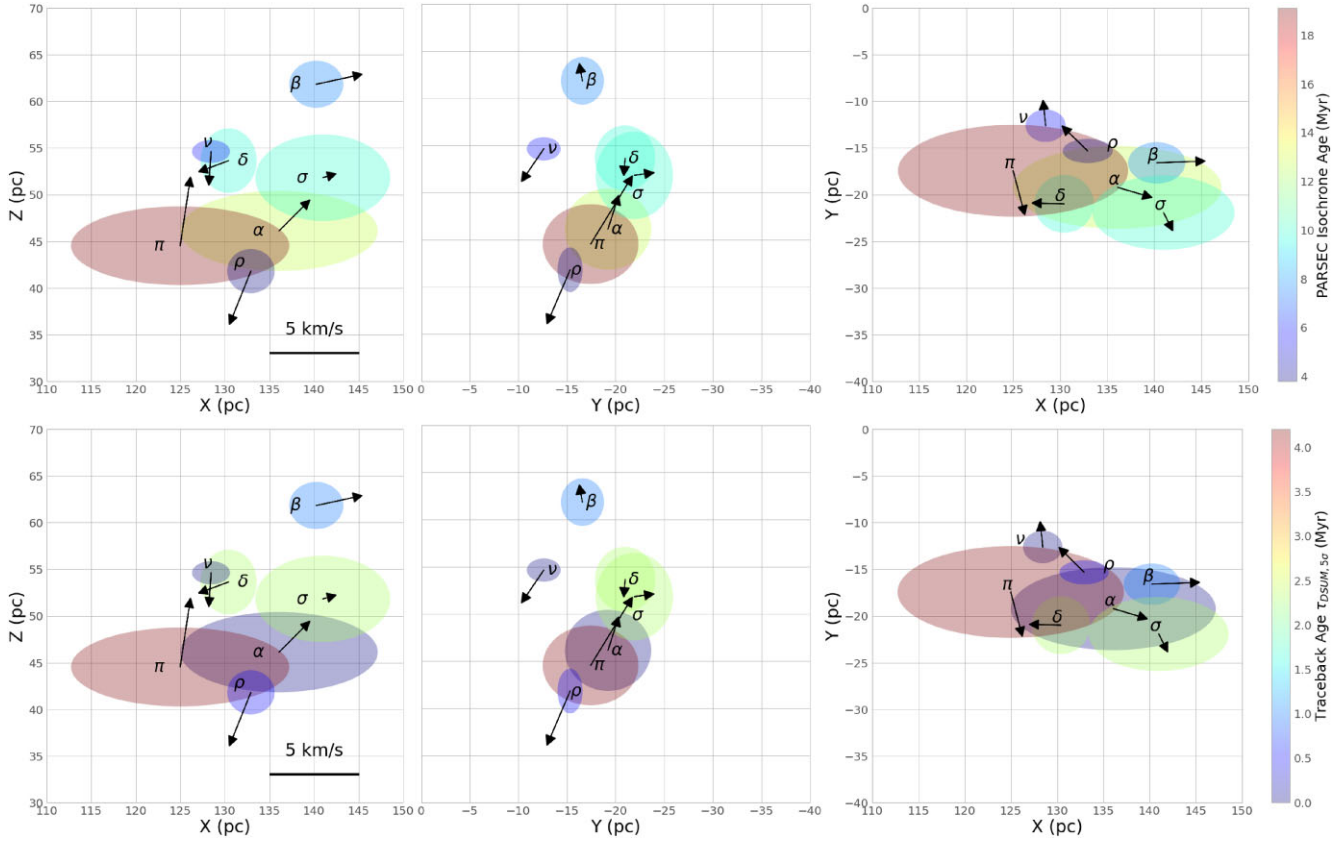

Figure 20. 3D Cartesian positions of Upper Scorpius subgroups represented by ellipses, the central coordinates and length of the semi-major and semi-minor axes which are given as the median coordinates (XYZ) and twice the dispersions ($\sigma_X, \sigma_Y, \sigma_Z$), respectively. The ellipses are labelled with the greek letters pertaining to the names given in Miret-Roig et al. (2022b) and colour-coded according to ages estimated in Ratzenböck et al. (2023b) using PARSEC stellar evolution models (Marigo et al. 2017) with *Gaia* BP–RP colour in the *top* panel, and traceback ages $\tau_{\rm DSum}$ in the *bottom* panel. Arrows indicate the average 3D velocities of each group relative to each other, with a scalebar in the rightmost panel.

ν Sco) also imply initially sparse distributions in large volumes, which may be incompatible with subgroup formation as 'clusters' embedded within 'pillars' of gas (Posch et al. 2025). This is closer to the picture of 'low density' star formation advocated for OB associations such as Cygnus OB2 by e.g. Wright et al. (2014).

Large initial volumes for subgroups also suggests a star-formation scenario where the triggering mechanism, such as via a cloud–cloud collision (e.g. Tan 2000; Wu et al. 2017) or via stellar feedback (e.g. Farias et al. 2024), impacts a large surface area of molecular cloud at a similar time, producing a sparse distribution of coeval young stars. This implies a greater distance between the feedback-driving source and the impacted region of molecular cloud.

Together, these results better support scenarios in which star formation in Upper Sco is either initiated spontaneously via development of instabilities in a GMC or else via large-scale external triggering, such as via a GMC–GMC collision or from external stellar feedback, or some combination of these modes.

For the GMC–GMC collision scenario, the range in ages of the subgroups would be expected to be similar to the GMC crossing time at the collision speed, i.e. $t_{\rm age\ spread} \sim D_{\rm GMC}/v_{\rm coll} \sim 100\,{\rm pc}/10\,{\rm km\,s^{-1}} \sim 10$ Myr. Such a scenario could lead to a coherent large-scale gradient in ages, i.e. as different parts of the cloud are engulfed in the collision. It could also lead to disturbed (unbound) kinematics of individual sub-groups.

For the external stellar feedback scenario, triggering may be from sources in the adjacent Upper Centaurus-Lupus (UCL) region, such as multiple likely past supernovae (see Krause et al. 2018). However, the formation of distinct subgroups within Upper Sco at different times due to this feedback impacting different regions of molecular gas at different times and with differing intensity, initiating star formation later in regions further from the feedback driving sources (e.g. ν Sco and ρ Oph), rather than star formation being triggered by feedback from previous generations in sequence within Upper Sco itself.

This scenario is similar to that recently proposed by Kerr et al. (2025) to explain the observed kinematic and age structure they identified in the Circinus star forming complex. In particular, they make comparison of their observations to the outputs of fiducial STARFORGE simulations (Grudić et al. 2021; Guszejnov et al. 2022), which have previously been shown to produce unbound and expanding populations similar to observed OB associations (Farias et al. 2024), and find that the scenario of 'inside-out' sequential star formation driven by feedback from a central cluster can produce the structures and age gradient found in Circinus and also in γ Vel & Vela OB2 (Pang et al. 2021; Armstrong et al. 2022).

However, the difference between Circinus, Vela OB2, and Upper Sco is the lack of a central dense cluster within Upper Sco which would have driven feedback across the region, as ASCC 79 and γ Vel are hypothesized to have done in Circinus and Vela OB2 respectively. Rather, the trends seen in these regions align better when considering

Table 3. Expansion gradients fitted for each group and in each dimension. Significance values listed are calculated from the ratio of the gradient to the uncertainty on the gradient, rounded down to the nearest integer.

	Velocity–Position pair	Gradient ($km\,s^{-1}\,pc^{-1}$)	Sig.	Timescale (Myr)	Aniso.
α	U X	$-0.000^{+0.005}_{-0.005}$	-		
	V Y	$0.036^{+0.009}_{-0.009}$	4σ	$28.4^{+9.8}_{-5.7}$	6σ
	W Z	$-0.047^{+0.010}_{-0.010}$	4σ		
β	U X	$0.105^{+0.026}_{-0.028}$	3σ		
	V Y	$0.131^{+0.018}_{-0.019}$	6σ	$7.8^{+1.3}_{-0.9}$	1σ
	W Z	$0.099^{+0.023}_{-0.023}$	4σ		
δ	U X	$0.120^{+0.020}_{-0.021}$	5σ		
	V Y	$0.110^{+0.008}_{-0.009}$	12σ		
	W Z	$0.165^{+0.008}_{-0.010}$	16σ	$6.2^{+0.4}_{-0.3}$	4σ
ν	U X	$-0.079^{+0.045}_{-0.044}$	1σ		
	V Y	$0.075^{+0.024}_{-0.025}$	3σ		
	W Z	$0.084^{+0.073}_{-0.074}$	1σ	$12.2^{+90.1}_{-5.7}$	1σ
π	U X	$0.033^{+0.008}_{-0.009}$	3σ		
	V Y	$0.006^{+0.011}_{-0.011}$	-		
	W Z	$0.064^{+0.017}_{-0.017}$	3σ	$16.0^{+5.8}_{-3.4}$	2σ
ρ	U X	$0.040^{+0.034}_{-0.036}$	1σ		
	V Y	$0.004^{+0.055}_{-0.054}$	-		
	W Z	$0.172^{+0.038}_{-0.039}$	4σ	$6.0^{+1.7}_{-1.1}$	2σ
σ	U X	$0.083^{+0.014}_{-0.015}$	5σ		
	V Y	$0.206^{+0.016}_{-0.017}$	12σ	$5.0^{+0.5}_{-0.4}$	5σ
	W Z	$0.073^{+0.020}_{-0.020}$	3σ		

Upper Sco as a part of Sco-Cen, with the central feedback-driving cluster being UCL.

In future work based on this survey data, we will investigate the origins of the 84 YSOs with kinematics distinct from any major subgroup, particularly as candidate runaway stars. We will compare a variety of kinematic age estimates for subgroups to ages derived from fitting stellar evolution models as well as Li-depletion models. We will also calculate mass accretion rates for YSOs and investigate trends between accretion, stellar mass and age.

7 SUMMARY

(i) We have carried out spectroscopic observations of >7000 targets selected from the *Gaia* DR3 source catalogue within 25 2°-diameter fields across the young nearby Upper Scorpius association using the 2dF/HERMES spectrograph at the AAT.

(ii) We reduce and analyse the spectra in order to derive radial velocities and youth indicators such as EW(Li)s, which we obtain for 6727 and 6937 unique sources, respectively.

(iii) We identify YSOs on the basis of EW(Li)s, H α emission and optical variability flagged in *Gaia* DR3. We identify 1204 confirmed YSOs.

(iv) We filter our YSO sample on *Gaia* astrometric quality criteria, leaving us with a sample of 544 confirmed YSOs with full reliable 6D kinematic information.

(v) We cross-match our confirmed YSOs with recent literature samples of Upper Scorpius members from Luhman & Esplin (2020); Miret-Roig et al. (2022b); Ratzenböck et al. (2023b) and match 1009, 1030, and 1085 of their samples, respectively, whilst also identifying >100 new YSOs in our sample.

(vi) We derive 3D heliocentric Cartesian positions XYZ and velocities UVW for our confirmed YSOs from observed astrometry.

(vii) We allocate our confirmed YSOs into the 7 kinematically distinct subgroups of Upper Sco as defined by Miret-Roig et al. (2022b), but we are also left with 84 YSOs whose kinematics are distinct from any of these groups by $>3\sigma$ which we consider separately as candidate ejected stars.

(viii) We estimate 3D velocity dispersions for each kinematic subgroup using a Bayesian approach with randomly sampled RV offsets from a simulated binary population. We find that velocity dispersions for most subgroups are significantly ($>3\sigma$) anisotropic, indicating that the subgroups retain much of their initial kinematic substructure and have not yet undergone sufficient dynamical mixing to develop isotropy. This is a commonly observed feature of OB associations and their subgroups (Wright 2020).

(ix) We then use the 3D velocity dispersions to estimate virial masses for the subgroups and compare them to masses estimated by extrapolation from a Kroupa et al. (2001) IMF. Virial mass estimates for all subgroups are significantly larger than those estimated by IMF extrapolation, in some cases by an order of magnitude, indicating that the subgroups are gravitationally unbound, as expected for OB associations.

(x) We calculate expansion velocities v_{out} and find that they are positive above uncertainties for all subgroups with varying levels of significance. In particular, the ρ Oph subgroup, often considered to be a bound young cluster, has a positive v_{out} of $>3.5\sigma$ significance and 72 per cent of its members moving outward from the central position. This is in contrast to the recent observation that Rho Oph is contracting (Wright et al. 2024).

Table 4. Rotation gradients for each group derived from fitting linear gradients between position and velocity in different dimensions.

Group	Velocity	Position	Gradient (km s^{-1} pc^{-1})	Signif.
α	V	X	$-0.022^{+0.004}_{-0.004}$	5σ
	W	X	$0.019^{+0.004}_{-0.004}$	4σ
	U	Y	$0.009^{+0.013}_{-0.012}$	–
	W	Y	$-0.037^{+0.010}_{-0.009}$	3σ
	U	Z	$-0.031^{+0.012}_{-0.012}$	2σ
	V	Z	$-0.053^{+0.009}_{-0.009}$	5σ
β	V	X	$-0.081^{+0.017}_{-0.017}$	4σ
	W	X	$0.005^{+0.020}_{-0.021}$	–
	U	Y	$0.001^{+0.032}_{-0.033}$	–
	W	Y	$-0.046^{+0.024}_{-0.023}$	1σ
	U	Z	$0.005^{+0.032}_{-0.032}$	–
	V	Z	$0.009^{+0.025}_{-0.024}$	–
δ	V	X	$-0.036^{+0.012}_{-0.012}$	3σ
	W	X	$0.014^{+0.017}_{-0.017}$	–
	U	Y	$0.049^{+0.023}_{-0.023}$	2σ
	W	Y	$-0.044^{+0.018}_{-0.017}$	2σ
	U	Z	$-0.004^{+0.018}_{-0.018}$	–
	V	Z	$-0.047^{+0.010}_{-0.010}$	4σ
ν	V	X	$-0.106^{+0.018}_{-0.018}$	5σ
	W	X	$0.015^{+0.046}_{-0.047}$	–
	U	Y	$-0.017^{+0.054}_{-0.053}$	–
	W	Y	$-0.043^{+0.056}_{-0.053}$	–
	U	Z	$-0.087^{+0.075}_{-0.076}$	1σ
	V	Z	$-0.008^{+0.036}_{-0.037}$	–
π	V	X	$0.005^{+0.005}_{-0.005}$	1σ
	W	X	$0.012^{+0.006}_{-0.006}$	2σ
	U	Y	$0.007^{+0.021}_{-0.022}$	–
	W	Y	$-0.054^{+0.014}_{-0.014}$	3σ
	U	Z	$-0.008^{+0.025}_{-0.024}$	–
	V	Z	$-0.006^{+0.014}_{-0.013}$	–
ρ	V	X	$0.011^{+0.028}_{-0.029}$	–
	W	X	$0.073^{+0.033}_{-0.035}$	2σ
	U	Y	$-0.187^{+0.067}_{-0.062}$	2σ
	W	Y	$-0.010^{+0.065}_{-0.064}$	–
	U	Z	$-0.133^{+0.038}_{-0.037}$	3σ
	V	Z	$0.040^{+0.030}_{-0.031}$	1σ
σ	V	X	$-0.060^{+0.013}_{-0.012}$	4σ
	W	X	$0.063^{+0.011}_{-0.012}$	5σ
	U	Y	$-0.044^{+0.029}_{-0.030}$	1σ
	W	Y	$-0.132^{+0.024}_{-0.024}$	5σ
	U	Z	$0.046^{+0.025}_{-0.025}$	1σ
	V	Z	$-0.038^{+0.022}_{-0.022}$	1σ

(xi) We find evidence for expansion ($> 3\sigma$ positive gradients) in at least one direction in all 7 groups, and evidence for contraction in α Sco and ν Sco. β Sco, δ Sco, and σ Sco exhibit significant expansion trends in all directions, while the trends of α Sco, β Sco, and σ Sco are significantly ($> 4\sigma$) anisotropic. For α Sco, β Sco, and σ Sco, the greatest rate of expansion is in the direction of Galactic rotation Y, while for δ Sco, ν Sco, π Sco, and ρ Oph, the greatest rate of expansion is in the direction perpendicular to the Galactic plane Z.

(xii) From the linear expansion gradients we also derive expansion timescales for each group, of $28.42^{+9.47}_{-5.68}$, $7.81^{+1.32}_{-0.94}$, $6.20^{+0.40}_{-0.29}$, $12.18^{+90.12}_{-5.66}$, $15.98^{+5.78}_{-3.35}$, $5.95^{+1.74}_{-1.08}$, and $4.97^{+0.45}_{-0.36}$ Myr, respectively. For β Sco, δ Sco, ρ Oph, and σ Sco these are comparable with literature age estimates.

(xiii) By fitting linear gradients to perpendicular position and velocity pairs we can also detect rotation trends. We find evidence ($> 3\sigma$) of rotation in all 7 subgroups of Upper Sco.

(xiv) We use an epicycle approximation and orbital equations to estimate the positions of YSOs up to 10 Myr in the past and thus trace the past evolution of the Upper Sco subgroups. We also use MST total length ($\tau_{\rm MSTlength}$; Squicciarini et al. 2021) and summed 3D distance ($\tau_{\rm DSum}$; Quintana & Wright 2022) metrics to estimate when subgroups would have been at their most compact configurations in the past, assumed to be approximately their initial configurations. α Sco and ν Sco, which previously showed evidence for contraction, are found to be approaching their most compact configurations in the near future. For the other subgroups which are expanding overall, we derive non-zero kinematic ages of $1.0^{+0.4}_{-0.4}$, $2.3^{+0.3}_{-0.3}$, $4.2^{+0.8}_{-0.8}$, $0.5^{+0.2}_{-0.2}$ and $2.3^{+0.5}_{-0.4}$ Myr, respectively. Except for ρ Oph, these are consistently significantly younger than the expansion time-scales derived by Miret-Roig et al. (2022b).

(xv) We estimate the sizes of subgroups at the past times when they would have been in their most compact configurations. We find that all subgroups would likely have had initial radii > 4 pc, which seems inconsistent with formation in 'cometary-shape' or 'pillars' of molecular gas of typical diameter ~ 1 pc and is more consistent with the extended, low-density view of OB association formation advocated by Wright et al. (2014) for Cygnus OB2.

(xvi) We compare the results of our kinematic analyses with those in recent literature as well as literature ages for the subgroups estimated by fitting PMS isochrones. We find that our dynamical ages estimates for the subgroups, as well as those from recent literature, are significantly younger than isochronal age estimates, which is problematic for the 'cluster-chain' sequential formation scenario.

(xvii) We assess the results of our analysis and we propose that a star formation scenario where feedback from the older UCL region of Sco–Cen initiated star formation at different times in different locations of Upper Sco, creating the age gradient seen among the distinct subgroups. The low intensity of feedback from the relatively distant UCL region, impacting a large surface area of molecular gas in Upper Sco over an extended period, resulted in initially sparse subgroups which have largely retained their initial kinematic structure.

ACKNOWLEDGEMENTS

JJA & JCT acknowledge support from ERC Advanced Grant MSTAR (788829). This project has also received funding from the European Union's Horizon 2020 research and innovation programme under grant agreement No 101004719. This material reflects only the authors views and the Commission is not liable for any use that may be made of the information contained therein. This work has made use of data from the ESA space mission *Gaia* (http://www.cosmos.esa.int/gaia), processed by the *Gaia* Data Processing and Analysis Consortium (DPAC, http://www.cosmos.esa.int/web/gaia/dpac/consortium). Funding for DPAC has been provided by national institutions, in particular the institutions participating in the *Gaia* Multilateral Agreement. This research made use of the Simbad and Vizier catalogue access tools (provided by CDS, Strasbourg,

France), Astropy (Astropy Collaboration et al. 2013) and TOPCAT (Taylor 2005).

DATA AVAILABILITY

The data underlying this article, both the spectroscopic parameters for observed targets and the astrometric parameters for confirmed PMS members will be available at CDS via https://cdsarc.unistra.fr/viz-bin/cat/J/MNRAS.

REFERENCES

AAO Software Team, 2015, Astrophysics Source Code Library, record ascl:1505.015
Ahumada R. et al., 2020, ApJS, 249, 3
Ambartsumian V., 1947, Acad. Sci. Armenian SSR, Yerevan
Armstrong J. J., Tan J. C., 2024, A&A, 692, A166
Armstrong J. J., Wright N. J., Jeffries R. D., Jackson R. J., Cantat-Gaudin T., 2022, MNRAS, 517, 5704
Astropy Collaboration et al., 2013, A&A, 558, A33
Bailer-Jones C. A. L., Rybizki J., Fouesneau M., Demleitner M., Andrae R., 2021, AJ, 161, 147
Baraffe I., Homeier D., Allard F., Chabrier G., 2015, A&A, 577, A42
Blaauw A., 1964, ARA&A, 2, 213
Buder S. et al., 2021, MNRAS, 506, 150
Buder S. et al., 2024, Pub. Astron. Soc. Aust., 42, 42
Cantat-Gaudin T., Mapelli M., Balaguer-Núñez L., Jordi C., Sacco G., Vallenari A., 2019a, A&A, 621, A115
Cantat-Gaudin T., Mapelli M., Balaguer-Núñez L., Jordi C., Sacco G., Vallenari A., 2019b, A&A, 621, A115
Chabrier G., 2003, PASP, 115, 763
Damiani F. et al., 2014, A&A, 566, A50
de Zeeuw P. T., Hoogerwerf R., de Bruijne J. H. J., Brown A. G. A., Blaauw A., 1999, AJ, 117, 354
Damiani F., Prisinzano L., Pillitteri I., Micela G., Sciortino S., 2019, A&A, 623, A112
El-Badry K., Rix H.-W., Heintz T. M., 2021, MNRAS, 506, 2269
Elmegreen B. G., Lada C. J., 1977, ApJ, 214, 725
Fabricius C. et al., 2021, A&A, 649, A5
Farias J. P., Offner S. S. R., Grudić M. Y., Guszejnov D., Rosen A. L., 2024, MNRAS, 527, 6732
Feast M., Whitelock P., 1997, MNRAS, 291, 683
Fiorellino E. et al., 2024, A&A, 686, A160
Foreman-Mackey D., Hogg D. W., Lang D., Goodman J., 2013, PASP, 125, 306
Fortune-Bashee X., Sun J., Tan J. C., 2024, ApJ, 977, L6
Frasca A., Biazzo K., Alcalá J. M., Manara C. F., Stelzer B., Covino E., Antoniucci S., 2017, A&A, 602, A33
Fuchs B., Breitschwerdt D., de Avillez M. A., Dettbarn C., Flynn C., 2006, MNRAS, 373, 993
Gaia Collaboration 2016, A&A, 595, A1
Gaia Collaboration, 2021, A&A, 649, A1
Gilmore G. et al., 2012, The Messenger, 147, 25
Gilmore G. et al., 2022, A&A, 666, A120
Goodwin S. P., Bastian N., 2006, MNRAS, 373, 752
Grudić M. Y., Guszejnov D., Hopkins P. F., Offner S. S. R., Faucher-Giguère C.-A., 2021, MNRAS, 506, 2199
Guszejnov D., Markey C., Offner S. S. R., Grudić M. Y., Faucher-Giguère C.-A., Rosen A. L., Hopkins P. F., 2022, MNRAS, 515, 167
Hennebelle P., Chabrier G., 2011, ApJ, 743, L29
Hills J. G., 1980, ApJ, 235, 986
Holmberg J., Flynn C., 2004, MNRAS, 352, 440
Inutsuka S.-i., Inoue T., Iwasaki K., Hosokawa T., 2015, A&A, 580, A49
Jackson R. J., Deliyannis C. P., Jeffries R. D., 2018, MNRAS, 476, 3245
Jeffries R. D., Jackson R. J., Sun Q., Deliyannis C. P., 2021, MNRAS, 500, 1158
Johnson D. R. H., Soderblom D. R., 1987, AJ, 93, 864
Karim M. T., Mamajek E. E., 2017, MNRAS, 465, 472
Kerr R., Farias J. P., Prato L., Rector T. A., Speagle J. S., Kraus A. L., 2025, ApJ, 985, 21
Kos J. et al., 2019, A&A, 631, A166
Kounkel M. et al., 2018, AJ, 156, 84
Krause M. G. H. et al., 2018, A&A, 619, A120
Kroupa P., 2001, MNRAS, 322, 231
Kroupa P., Aarseth S., Hurley J., 2001, MNRAS, 321, 699
Krumholz M. R., McKee C. F., 2005, ApJ, 630, 250
Kuhn M. A., Hillenbrand L. A., Sills A., Feigelson E. D., Getman K. V., 2019, ApJ, 870, 32
Kurucz R. L., 1992, in Barbuy B., Renzini A., eds, IAU Symposium Vol. 149, The Stellar Populations of Galaxies. Kluwer Academic Publishers, Dordrecht, p. 225
Lada C. J., Lada E. A., 2003, ARA&A, 41, 57
Lewis I. J. et al., 2002, MNRAS, 333, 279
Li Q., Tan J. C., Christie D., Bisbas T. G., Wu B., 2018, PASJ, 70, S56
Lindegren L. et al., 2021, A&A, 649, A4
Loren R. B., 1989, ApJ, 338, 902
Luhman K. L., 2022, AJ, 163, 24
Luhman K. L., Esplin T. L., 2020, AJ, 160, 44
Majewski S. R. et al., 2017, AJ, 154, 94
Mapelli M., 2017, MNRAS, 467, 3255
Marigo P. et al., 2017, ApJ, 835, 77
Marton G. et al., 2023, A&A, 674, A21
Maschberger T., 2013, MNRAS, 429, 1725
Miao J., White G. J., Nelson R., Thompson M., Morgan L., 2006, MNRAS, 369, 143
Miret-Roig N. et al., 2022a, Nat. Astron., 6, 89
Miret-Roig N., Galli P. A. B., Olivares J., Bouy H., Alves J., Barrado D., 2022b, A&A, 667, A163
Miret-Roig N., Alves J., Barrado D., Burkert A., Ratzenböck S., Konietzka R., 2024, Nat. Astron., 8, 216
Padoan P., Nordlund Å., 2011, ApJ, 730, 40
Palla F., Randich S., Flaccomio E., Pallavicini R., 2005, ApJ, 626, L49
Pang X., Yu Z., Tang S.-Y., Hong J., Yuan Z., Pasquato M., Kouwenhoven M. B. N., 2021, ApJ, 923, 20
Parker R. J., Goodwin S. P., Kroupa P., Kouwenhoven M. B. N., 2009, MNRAS, 397, 1577
Pecaut M. J., Mamajek E. E., 2016, MNRAS, 461, 794
Posch L., Miret-Roig N., Alves J. a., Ratzenböck S., Großschedl J., Meingast S., Zucker C., Burkert A., 2023, A&A, 679, L10
Posch L., Alves J., Miret-Roig N., Ratzenböck S., Großschedl J., Meingast S., Swiggum C., Konietzka R., 2025, A&A, 693, A175
Preibisch T., Mamajek E., 2008, in Reipurth B.ed., Vol. 5, Handbook of Star Forming Regions, Volume II. Astron. Soc. Pac., San Francisco, p. 235
Quintana A. L., Wright N. J., 2022, MNRAS, 515, 687
Raghavan D. et al., 2010, ApJS, 190, 1
Randich S. et al., 2022, A&A, 666, A121
Ratzenböck S., Großschedl J. E., Möller T., Alves J., Bomze I., Meingast S., 2023a, A&A, 677, A59
Ratzenböck S. et al., 2023b, A&A, 678, A71
Rigliaco E. et al., 2016, A&A, 588, A123
Schönrich R., Binney J., Dehnen W., 2010, MNRAS, 403, 1829
Scoville N. Z., Sanders D. B., Clemens D. P., 1986, ApJ, 310, L77
Sheinis A. et al., 2015, J. Astron. Telesc. Instrum. Syst., 1, 035002
Sills A., Rieder S., Scora J., McCloskey J., Jaffa S., 2018, MNRAS, 477, 1903
Sneden C., Bean J., Ivans I., Lucatello S., Sobeck J., 2012, Astrophysics Source Code Library, record ascl:1202.009
Soderblom D. R., 2010, araa, 48, 581
Squicciarini V., Gratton R., Bonavita M., Mesa D., 2021, MNRAS, 507, 1381
Suwannajak C., Tan J. C., Leroy A. K., 2014, ApJ, 787, 68
Tan J. C., 2000, ApJ, 536, 173
Tan J. C., 2010, ApJ, 710, L88

Tan J. C., Shaske S. N., Van Loo S., 2013, in Wong T., Ott J., eds, IAU Symposium Vol. 292, Molecular Gas, Dust, and Star Formation in Galaxies. Kluwer, Dordrecht, p. 19
Tasker E. J., Tan J. C., 2009, ApJ, 700, 358
Taylor M. B., 2005, in Shopbell P., Britton M., Ebert R., eds, ASP Conf. Ser. Vol. 347, Astronomical Data Analysis Software and Systems XIV, Astron. Soc. Pac., San Francisco, p. 29
Tsantaki M. et al., 2022, A&A, 659, A95
Tutukov A. V., 1978, A&A, 70, 57
Wright N. J., 2020, New A Rev., 90, 101549
Wright N. J., Mamajek E. E., 2018, MNRAS, 476, 381
Wright N. J., Parker R. J., Goodwin S. P., Drake J. J., 2014, MNRAS, 438, 639
Wright N. J., Bouy H., Drew J. E., Sarro L. M., Bertin E., Cuillandre J.-C., Barrado D., 2016, MNRAS, 460, 2593
Wright N. J., Kounkel M., Zari E., Goodwin S., Jeffries R. D., 2023, in Inutsuka S., Aikawa Y., Muto T., Tomida K., Tamura M., eds, ASP Conf. Ser. Vol. 534, Protostars and Planets VII. Astron. Soc. Pac., San Francisco, p. 129
Wright N. J. et al., 2024, MNRAS, 533, 705
Wu B., Tan J. C., Christie D., Nakamura F., Van Loo S., Collins D., 2017, ApJ, 841, 88
Wu B., Tan J. C., Nakamura F., Christie D., Li Q., 2018, PASJ, 70, S57
Wu B., Tan J. C., Christie D., Nakamura F., 2020, ApJ, 891, 168
Zari E., Brown A. G. A., de Zeeuw P. T., 2019, A&A, 628, A123
Zwart S. P., McMillan S., Gieles M., 2010, ARA&A, 48, 431
Zwitter T. et al., 2018, MNRAS, 481, 645

This paper has been typeset from a TEX/LATEX file prepared by the author.